

Brief communication: Seismological analysis of flood dynamics and hydrologically-triggered earthquake swarms associated with Storm Alex

Małgorzata Chmiel^{1,2,6}, Maxime Godano¹, Marco Piantini³, Pierre Brigode^{1,5}, Florent Gimbert³, Maarten Bakker³, Françoise Courboulex¹, Jean-Paul Ampuero¹, Diane Rivet¹, Anthony Sladen¹, David Ambrois¹, and Margot Chapuis⁴

¹Université Côte d'Azur, Observatoire de la Côte d'Azur, Géoazur, CNRS, IRD, Sophia Antipolis, France

²Laboratory of Hydraulics, Hydrology and Glaciology, ETH Zürich, Zürich, Switzerland

³Institute for Geosciences and Environmental Research (IGE), CNRS / INSU, IRD, University Grenoble Alpes and Grenoble-INP, Grenoble, France

⁴Université Côte d'Azur, CNRS, ESPACE, bd Edouard Herriot, 06204 Nice, France

⁵Université Paris-Saclay, INRAE, UR HYCAR, 1 Rue Pierre-Gilles de Gennes, 92160 Antony, France

⁶Swiss Federal Institute for Forest, Snow and Landscape Research, Zürich, Switzerland

Correspondence: malgorzata.chmiel@wsl.ch

Abstract.

On October 2, 2020, the Maritime Alps in southern France were struck by devastating Storm Alex that caused locally more than 600 mm of rain in less than 24 hours. The extreme rainfall and flooding destroyed regional rain and stream gauges. That hinders our understanding of the spatial and temporal dynamics of rainfall-runoff processes during the storm. Here, we show that seismological observations from permanent seismic stations constrain these processes at a catchment scale. The analysis of seismic power, peak frequency, and backazimuth provide us with the timing and velocity of the propagation of flash-flood waves associated with bedload-dominated phases of the flood on the Vésubie river. Moreover, the combined short-term average to long-term average ratio and template matching earthquake detection reveal that 114 local earthquakes between local magnitude $ML=-0.5$ and $ML=2$ were triggered by the hydrological loading and/or the resulting in-situ underground pore pressure increase. This study shows the impact of Storm Alex on the Earth's surface and deep layer processes and paves the way to future works that can reveal further details of these processes.

1 Introduction

Extreme weather events might trigger an extreme response of the Earth's surface and subsurface processes, e.g., in the form of rapid and disastrous flash-floods (e.g., Khajehei et al., 2020), mass movements (Stoffel and Huggel, 2012), and/or seismogenic underground stress changes (e.g., Rigo et al., 2008). These processes contribute to societal and environmental risks and are an important agent in landscape evolution. Moreover, some extreme weather events might become more frequent due to climate change (IPCC, In Press.). That is why it is crucial to reliably quantify the spatio-temporal response of the Earth's systems to extreme weather forcing.

Seismic methods have the potential to monitor surface and subsurface processes associated with extreme weather events. In particular, both turbulent flow and sediment transport during floods generate ground motion in different frequency bands (Schmandt et al., 2013; Gimbert et al., 2014) that can be used to track the flood dynamics (e.g., Cook et al., 2018). Surface seismic waves are generated by impact forces exerted by mobile particles on the river bed (e.g., Tsai et al., 2012; Gimbert et al., 2019) and ambient seismic measurements have recently been used to monitor fluxes associated with transported bed material (Bakker et al., 2020; Lagarde et al., 2021). In the past decade, near-river seismic monitoring has been conducted during moderate-magnitude floods (e.g., Burtin et al., 2016; Roth et al., 2016) and controlled small-magnitude flow events (Schmandt et al., 2013, 2017). To date, extensive seismic investigations of large-magnitude flood events are rare and mostly associated with glacier lake outburst floods (Cook et al., 2018; Maurer et al., 2020) and natural hazard cascade (Cook et al., 2021). Yet, improved understanding of flood dynamics is crucial for early warning, risk mitigation, and modeling landscape evolution (Raynaud et al., 2015; Borga et al., 2019).

Exceptionally intense rainfall can reactivate existing faults through changing crustal stress conditions due to additional fluid mass load or in situ stress changes, resulting in hydrologically triggered earthquakes (e.g., Hainzl et al., 2006). Over the past two decades, a growing number of studies has shown a correlation between meteorological events and earthquake activity in various geological contexts (Costain and Bollinger, 2010). Several sites show the seasonal modulation of the seismicity due to rainfall or snowmelt periods in Japan (Ueda and Kato, 2019); Nepal (Kundu et al., 2017); Taiwan (Hsu et al., 2021); Oregon, USA (Saar and Manga, 2003); California, USA (Johnson et al., 2017; Montgomery-Brown et al., 2019); and Italy (D'Agostino et al., 2018). Other observations display a punctual increase of seismic activity following an exceptional rainfall episode, for example in the Swiss Alps (Roth et al., 1992), German Alps (Kraft et al., 2006), and southern France (Rigo et al., 2008).

Here, we present a set of seismological observations from 11 stations from the permanent French RESIF Network that captured the October 2020 extreme rainfall and flash flood caused by Storm Alex (Carrega and Michelot, 2021) in the southwestern Alps (the Maritime Alps), South-East France. This unique dataset not only allows us to study surface flash-flood related hazard, but also the seismogenic subsurface response to an unusually intense rainfall which locally exceeded 600 mm in less than a day. Three rivers were strongly impacted by the flash floods: the Vésubie, the Roya, and the Tinée rivers (Figure 1A). We first gain insights onto the Vésubie river dynamics during the flash flood by analyzing seismic power, peak frequency, and dominant backazimuthal orientation of seismic noise. These observations are compared with simple rainfall-runoff modeling (Brigode et al., 2021a). Then, by using template matching we detect a series of impulsive signals that correspond to small earthquakes [down to local magnitude (ML) of -0.5] in the area where rainfall rate in the Tinée river catchment area was maximum. This preliminary analysis demonstrates that the seismological observations reported herein provide a better understanding and quantification of the hydro-geological impact of extreme weather phenomena on the mountainous terrain and the related fluvial hazards. The latter is important for catchment areas with few “classical” hydrological observations, as the Vésubie river catchment presented here.

2 Storm Alex: a very destructive “Mediterranean episode”

On October 2, 2020, the Maritime Alps were struck by a violent meteorological event called a “Mediterranean episode” caused by Storm Alex (Carrega and Michelot, 2021). Although heavy rainfalls occur regularly in autumn in the Mediterranean region, the Storm Alex maximum daily rainfall was the highest since the beginning of the rainfall measurements in 1997. The continuous regional rainfall COMEPHORE database used in this study started in 1997 (Figure 1C). The rainfall started at 06:00 UTC on October 2, 2020, lasted for less than 24 hours and generated a cumulative intensity that locally exceeded the typical yearly average (>600 mm/day, Figure 1A). These estimates have been obtained hourly with the ANTILOPE rainfall estimation (Laurantin, 2008) with 1 km^2 spatial resolution. The ANTILOPE model was produced by Météo-France and constrained by radar data and 40 rain gauges located in the region (Figure 1A). The locations of regional rain and stream gauges are shown in Figure B1. The estimation of rainfall maps is highly uncertain in this context due to few rain gauges available, rainfall measurement uncertainties due to observed intensities, limits of the radar observations, and spatial interpolation.

The torrential rains triggered hazardous flash floods and landslides of an intensity and spatial extent that have never been observed yet in this area, causing several casualties as well as large infrastructure and economic damage [Figure 1A, B2, Brigode et al. (2021b)]. To date, the spatial and temporal evolution of the flood remain poorly understood. This is partially due to a limited number of observations caused by the instrument destruction during the flood. Stream gauge measurements during the episode are incomplete and highly uncertain due to scale saturation, destruction of measuring devices, and changes in the river bed level.

We focus our flood-dynamics analysis on the Vésubie river because (1) the Vésubie catchment has been one of the most strongly affected in the region (Figure 1, B2, B3) and (2) the seismic station coverage is particularly suitable in this catchment with three seismic stations being located in the proximity: SPIF (3-component velocimeter), BELV (3-component accelerometer) and TURF (3-component velocimeter) at respectively about 1,570, 630 and 5,970 m from the Vésubie river. We investigate the level of seismic power recorded by these stations by calculating the Power Spectral Densities (PSD, Solomon (1991b)) during the storm. Then, we perform additional analysis on the SPIF station by assessing temporal changes in: (1) peak frequency, (2) dominant backazimuthal orientation of seismic noise, and (3) relation between high frequency (10-45 Hz) and low frequency (1-10 Hz) seismic noise. We contextualize these seismological observations by comparing them with rainfall estimations obtained with the ANTILOPE model and runoff temporal series. A simple KLEM rainfall-runoff model (Kinematic Local Excess Model, Borga et al. (2007)) is used for runoff simulation. A full description of the methods used in this paper is provided in Appendix A.

3 Results

80 3.1 Seismological observations associated with the flash flood

All three seismic stations (SPIF, BELV, and TURF) show elevated noise levels during the 24 h period starting at 07:00 UTC October 2, 2020, that overlap with the duration of Storm Alex (Carrega and Michelot, 2021) (Figure 1D). The stations SPIF and BELV show elevated seismic power (PSD) from $\sim 10:00$ UTC October 2 to $\sim 06:00$ UTC October 3 in the frequency band 1-20 Hz. The seismic power during Storm Alex is at least 20 dB up to about 30 dB higher than the pre-flood "background" ambient seismic noise power levels. Since the decibel scale is a base-10 logarithmic scale, a 20 dB observed difference means 100 times higher seismic power. For the TURF station, the seismic power increased by at least 100 times relative to the pre-flood conditions, especially at frequencies lower than 5 Hz. The seismic power averaged in the 1-20 Hz frequency band for SPIF and BELV stations (Figure 2A-B) show a rapid increase in recorded seismic power from 10:00 and 11:00 UTC, respectively. Three local seismic power maxima are visible on SPIF and BELV stations. They are marked in color in Figure 2 and the seismic power thresholds used to define the maxima are shown in Figure B4. We determine the thresholds manually; they delimit the values in seismic power when the seismic power strongly and rapidly increases. The maxima 1 and 2 are not marked in Figure 2C because we cannot identify them at the TURF station.

The first two seismic power maxima have pronounced high-amplitude peaks and arrive at 12:05 and 13:15 (SPIF), and 12:30 and 13:35 UTC (BELV), respectively. The third maximum has a distributed amplitude in time and occurs between $\sim 16:00$ and $\sim 20:00$ UTC at SPIF and $\sim 16:00$ and $\sim 22:00$ UTC at BELV. The seismic power recorded at the TURF station shows a progressive increase with a single broad peak between $\sim 17:30$ and $\sim 22:00$ UTC. The peak associated with the first maximum has the highest magnitude at the SPIF station, while all three maxima have similar magnitudes on the BELV station. The peak associated with the first maximum lasts for ~ 30 min and that associated with the second maximum lasts for ~ 90 min. The peak associated with the third maximum is the broadest, lasting for 4 and 6 hours on the SPIF and BELV stations, respectively. For the sake of comparison with the runoff modelling, we use a linear scale for the seismic power representation in Figure 2A, B4. For an alternative seismic power representation in decibels [$10 \log_{10}(\text{PSD})$] the reader can refer to Figure B4.

Runoff simulations show two runoff maxima at three analysed locations (Figure 2A-C). The analysed locations correspond to the river points with the shortest distance between the seismic stations and the Vésubie river and are shown in Figure B3A. Modelling predictions indicate that the runoff maxima occur at 14:00, 14:25, and 15:00 UTC (the first runoff maximum), and 18:00, 18:25, 19:00 UTC (the second runoff maximum), from upstream to downstream. The available stream gauge measurements at Utelle (Figure B3A) show a similar rapid increase in runoff as the seismic power and the rainfall-runoff model (Figure B5). However, no maximum runoff measurements are available since the stream gauge (marked as a dark-blue diamond in Figure 1A and B3A) was destroyed during the flood.

To investigate potential changes in seismic noise sources, we calculate the peak frequency and the backazimuth (Figure 2E-F). In Figure 2E peak frequency values are time color-coded meaning that each color corresponds to the consecutive 200 s long time windows shown in Figure 2A). The peak frequency corresponds to the frequency that has the maximum seismic power value in the analyzed time window (Figure B6D). Peak frequency and backazimuth (θ , averaged in the 3-8 Hz frequency

band, Figure 2F) show distinct value shift at the SPIF station before and during the flood. Starting from 08:30 UTC multiple lightning strikes occurred at the distance of 15 km from the SPIF station (<https://www.blitzortung.org/en/>, Figure B6). At 115 this time there are higher-amplitude arrivals visible at the SPIF station causing jumps in the peak frequency from 2 Hz to higher values up to 40-50 Hz at 09:30 UTC (Figure B6). These arrivals can be associated with the lightning/thunder, rain, or anthropogenic activity. However, at 11:00 UTC the peak frequency stabilizes at 6 Hz. Then, the peak frequency drops to 4 Hz at \sim 13:20 and comes back to 6 Hz at \sim 15:00 UTC. This drop in the peak frequency coincides in time with the second seismic power maximum visible at the SPIF station. The backazimuth starts pointing along a 100° - 120° axis at 10:00 UTC (Figure 2F) 120 although the degree of polarization is relatively weak ($\beta^2 \sim 0.5$, Figure B7). The dominant degree of polarization (β^2 in the range 0-1), based on Koper and Hawley (2010), provides a measure for the confidence with which the horizontal azimuth can be interpreted, where $\beta^2 > 0.5$ is recommended by Goodling et al. (2018). Therefore the backazimuth observations should be taken with caution.

The relative contributions of low- (2-10 Hz) and high- (10-45 Hz) frequency seismic power are shown in Figure 2G. Different 125 time periods characterized by a varying relationship between low frequency and high frequency seismic power can be identified: between 08:30 and 10:00 UTC the seismic power increases similarly in the two-frequency range (slope ~ 1), between 10:00 and 16:00 UTC the high frequency seismic power increases more strongly (slope > 1), and finally between 16:00 UTC October 2 and 07:00 UTC October 3 the seismic power decreases similarly. The equivalent of Figure 2G in the linear amplitude scale [(m/s) 2 Hz $^{-1}$] is presented in Figure B8. We discuss the significance of slope changes in the discussion section.

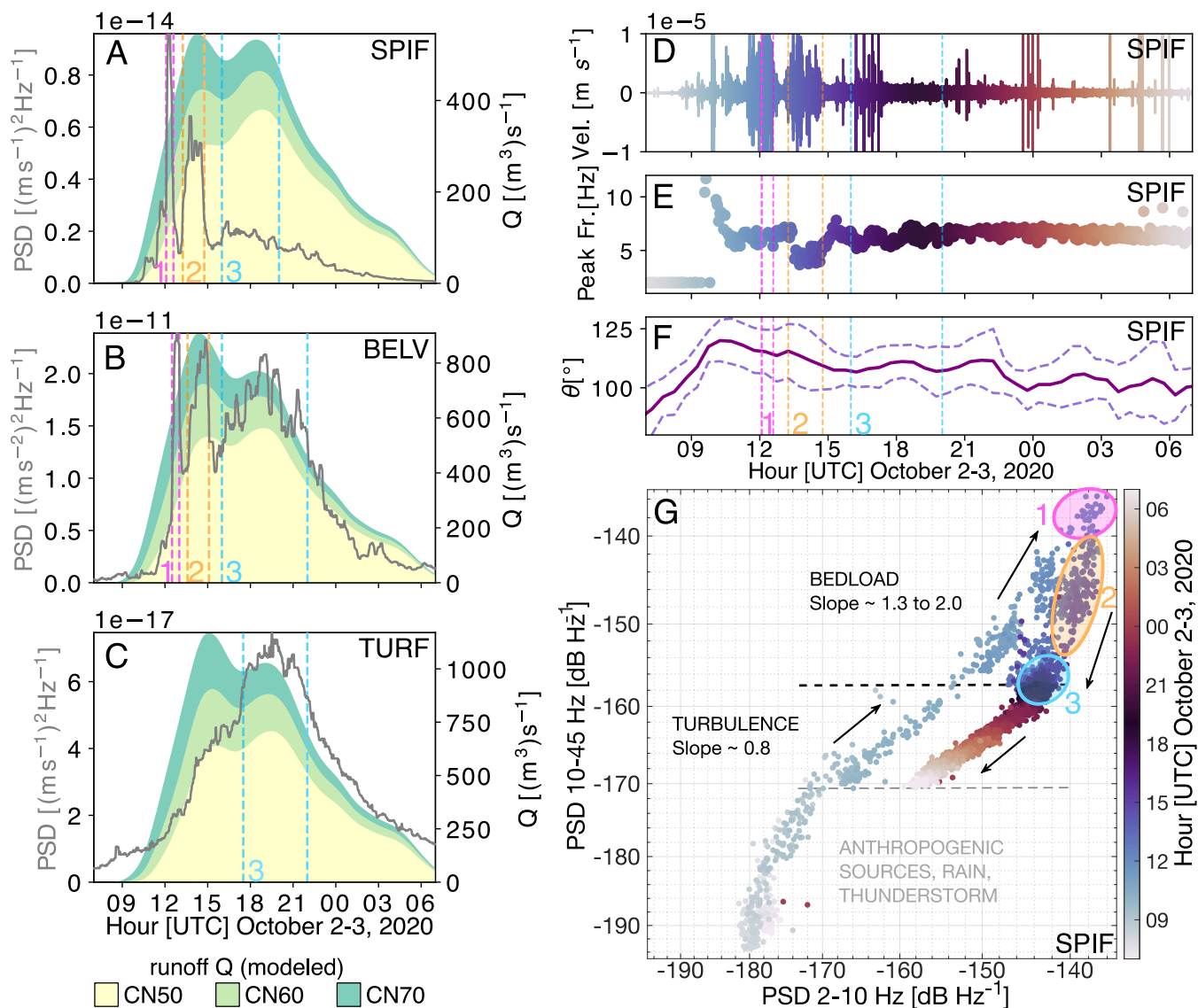


Figure 2. Analysis of continuous seismic signals recorded during Storm Alex. Seismic power (PSD) averaged between 1 and 20 Hz and recorded at stations A. SPIF, B. BELV, and C. TURF. The results of the runoff simulation are marked in yellow (CN60), light green (CN70), and green (CN80), where CN denotes three different basin saturation scenarios: CN70 (moderate saturation), CN60, and CN50 (rather dry conditions). Seismic power is smoothed with a moving time window of 30 min and the runoff is calculated with a 5-min time step. D. Vertical ground velocity recorded at the SPIF station filtered in 1-50 Hz. E. Peak frequency calculated for each 200 s segment. Peak frequency and corresponding time segment are marked in the same color. F. Backazimuth (smoothed over three 30-min consecutive time windows) calculated at the SPIF station averaged over 3-8 Hz and its standard deviations (dashed lines). G. Seismic power in the 2-10 Hz frequency band versus seismic power in 10-45 Hz at SPIF station. All results are shown from 07:00 UTC October 2 to 07:00 UTC October 3, 2020.

130 **3.2 Earthquake swarm detection**

Since 2014, the seismic activity of the studied area is permanently monitored by the Seiscomp3 (Hanka et al., 2010) system. A routine short-time average long-time average (STA/LTA) detection method is implemented in the SeisComp3 system, operating in Observatoire de la Côte d'Azur for the monitoring of the seismic activity in the South-Western Alps. For the past 7 years, the area of the Tinée valley has shown a regular monthly seismic activity with an average of 2 earthquakes of local magnitude
135 (ML) larger than 0.4 and transient increases up to 11 earthquakes (Figure 3). However, after Storm Alex, 23 earthquakes were detected, which is the highest monthly earthquake rate since 2014. This uncommon seismic activity consisted of 23 earthquakes located along the Tinée valley at around 4 km depth (Figure 3B-C). The seismic crisis started on October 4, 2020, about 24 hours after the end of Storm Alex, and lasted throughout October with small events in November and December (Figure 3D). The earthquakes form three distinct swarms in space and time that were mostly successively activated from South
140 to North (Figure 3B-C). The location error is estimated to be about ± 2 km. We detected 91 additional earthquakes by applying the template matching detection method (Gibbons and Ringdal, 2006) to the continuous data recorded by the MVIF station (Figure 3D). The template matching increases the number of detected earthquakes by about 400 % and decreases the minimum magnitude by one unit compared to the Seiscomp3 detections based on STA/LTA. Most of the newly identified events occur on October 8 and may be related to the central swarm since they best correlate with one of the templates constituting this cluster.

145 **4 Discussion**

4.1 The Vésubie river dynamics during the flash flood

Comparison amongst the increased seismic power (at least 100 up to 1,000 times larger than common noise levels), runoff modeling, and runoff measurements indicates that the signals recorded by the SPIF, BELV and TURF stations during Storm Alex are mostly generated by the flash flood on the Vésubie river. The rapid increase in seismic power, the changes in peak frequencies, and dominant backazimuth suggest the flash flood on the Vésubie river started at about 10:00 UTC. The backazimuth
150 values measured at the SPIF station points towards 110° direction (Figure B3, black arrow), which does not point towards the closest river section (located at a backazimuth of 66°). The backazimuth of $\sim 110^\circ$ may be associated with a bending of the Vésubie river channel, a ~ 2.5 km long downstream reach of the Vésubie river that aligns with the estimated azimuth, or the confluence of the Venanson stream with the Vésubie river which lies in the estimated direction (Figure B3B). This provides
155 evidence that the commonly made assumption that the recorded seismic signals are associated with the river segments located closest to the station (e.g., Roth et al., 2016; Zhang et al., 2021) may not be always valid.

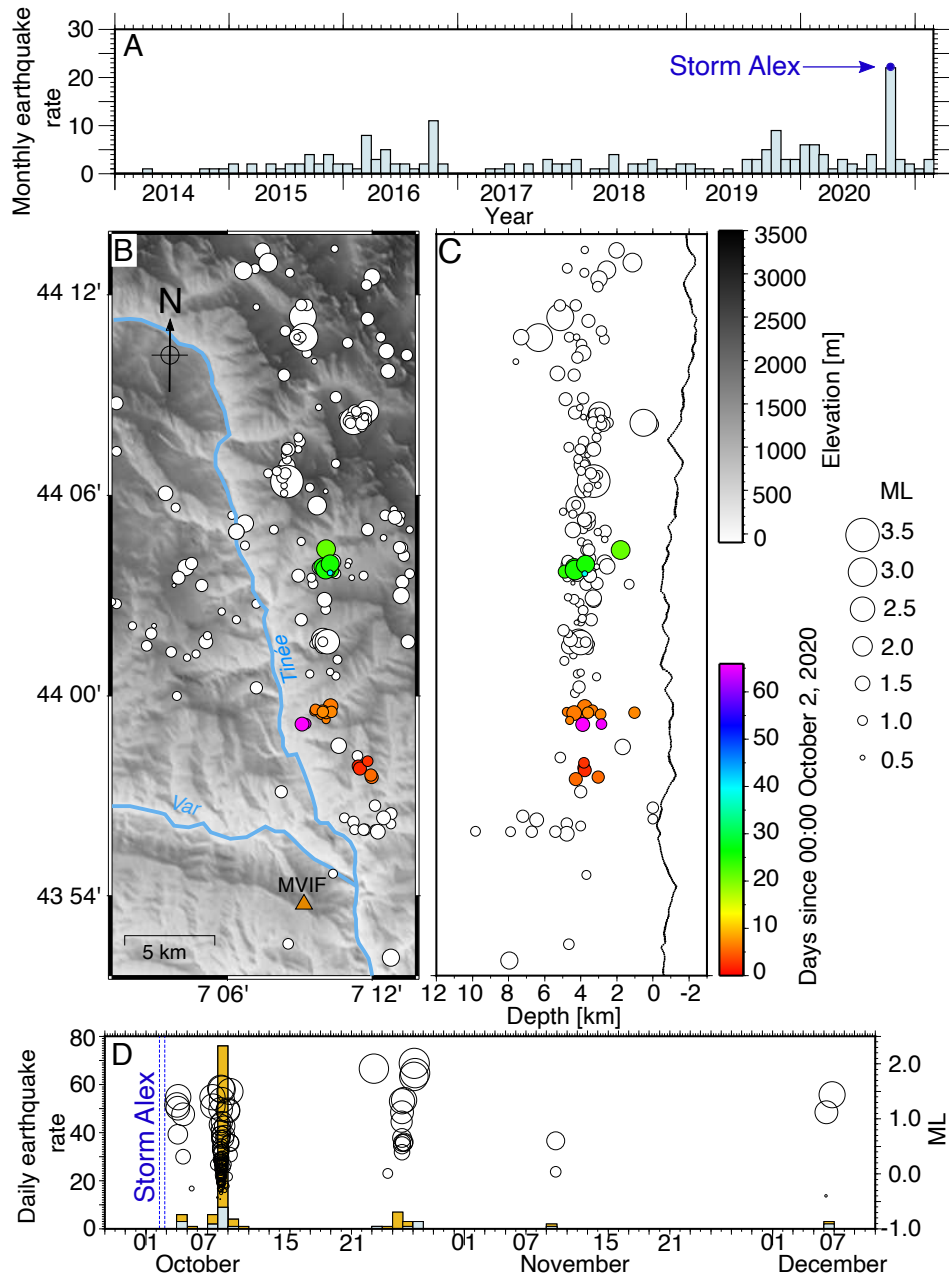


Figure 3. Seismic activity of the Tinée valley. A. Monthly seismic activity between January 2014 and March 2021 detected by the SeisComP3 system. The blue arrow indicates the occurrence of Storm Alex. B. Map of the seismicity over the period 2014-2021 located by SeisComP3 system. Colored circles are earthquakes following Storm Alex. White circles are background seismicity. Orange triangle represents the seismological broadband station MVIF. C. North-South cross section displaying the depth range of the seismicity with respect to the sea level and the line is the average elevation of the map in B. D. Daily rate (left axis) and local magnitude (right axis) for the seismic activity following Storm Alex. Grey bars are the number of earthquakes detected by the Seiscomp3 system. Orange bars are the number of earthquakes detected by template matching. Black circles represent the detected earthquakes. The size is proportional to the magnitude. Dashed blue lines indicate the duration of Storm Alex.

Both seismic power and peak frequency are site-dependent seismic parameters, i.e. they depend on seismic quality factor, the velocity of Rayleigh waves, and the source-station distance (Aki and Richards, 2002). However, according to a modified Tsai et al. (2012) model for hazardous flow monitoring from Lai et al. (2018), the seismic power is strongly sensitive to particle sediment size and flow speed, while the peak frequency mostly depends on the distance from the seismic source to the receiver. Also, previous observations reported no significant shift in peak frequency with varying runoff (Schmandt et al., 2013; Burtin et al., 2016). Therefore, the observed drop in the peak frequency (down to 4 Hz) that temporally correlates with the occurrence of the second seismic power maximum at the SPIF station (Figure 2A, E) can potentially be generated by a stronger more distant source. Indeed, the flash flood impacted the adjacent hill slopes through undercutting and destabilization of the riverbanks, leading to bank, road, and bridge collapses, and landslides distributed along the river network (Figure B2). Another possible explanation could be a tributary that becomes a dominant seismic source at this moment. However, the results of the rainfall-runoff modeling for large tributaries (Boréon and Madone de Fenestre river) do not confirm this hypothesis. Also, the backazimuth analysis does not show value changes during the second seismic power maximum. This can be due to (1) changes in the seismic source location that lie in the same general azimuthal direction, (2) the difference in time scale between backazimuth estimates made over 30 minutes versus peak frequency calculations made over 200 s windows, or, perhaps most likely, (3) the low degree of polarization of the surface waves due to spatial spread of the source or to wave scattering.

Since river flow turbulence is expected to preferentially generate ground motion at low frequencies compared to bedload transport (e.g., Burtin et al., 2011; Schmandt et al., 2013; Gimbert et al., 2014), the relationships between seismic power at low versus high frequencies can tell us whether our observations may be sensitive to bedload transport (Bakker et al., 2020). As the flood develops we observe a change in scaling between low- and high-frequency seismic power, materialized by a transition from a 0.8 to a 1.3 scaling exponent as high frequency seismic power becomes higher than -158 dB (Figure 2G). We interpret this observation as an indication that high frequency seismic power above the -158 dB threshold is mostly bedload induced. This is consistent with expectation of enhanced bedload transport from this stage onwards due to increased bed shear stress and/or the activation of additional sediment supply sources from river bed destabilization or bank erosion (Cook et al., 2018). Interestingly, after peak seismic energy has been reached, high frequency seismic power drops drastically compared to low frequency seismic power (with a scaling exponent of about 2), consistent with an abrupt decrease in sediment transport. Next, the low- versus high-frequency power scaling relation comes back to that observed during the early rising phase, consistent with higher frequencies over this time frame getting back to being mostly sensitive to water flow. We also note that after the flood, the low-frequency seismic power is higher compared to before the flood (~10 dB difference, see also the spectrogram of the SPIF station in Figure 1), which could be due to flood-induced changes in river bed geometry and/or flow conditions (e.g. river roughness, Roth et al. (2017)) that may preferentially affect low frequency power.

About six hours passed between the beginning of Storm Alex and the first flash-flood peak flow. The two seismic power maxima visible at the near-river stations (SPIF and BELV; the first maximum is marked in pink, and the second one in orange in Figures 2A, B and G) occurred in what we identified as the bedload transport phase in Figure 2G. Under the hypothesis that the two peaks associated with seismic power maxima represent the same moving source, we estimate their propagation velocity at 5.8 (± 1.2) m/s and 4.8 (± 1.5) m/s, respectively. The details of the velocity and the error propagation calculation are given

in appendix B. These peaks overlap in time with the first maximum of runoff simulations (Figure 2A-B). Such elevated and short-live peaks could be generated by flood waves. Similar peaks in seismic power generated by flood waves were observed during glacial lake outburst floods in the Himalayas by Cook et al. (2018) and Maurer et al. (2020). These peaks may also be associated with the passage of sediment pulses such as those experimentally investigated by Piantini et al. (2021) in a torrential river setting. Such pulses can be generated by external sediment inputs to the river, triggered by the sudden destabilization of debris deposits at the base of slopes and cliffs.

The absence of the two main maxima on the TURF station can be related to a lack of sensitivity of this station to the bedload transport due to its large distance from the river (~ 6 km). Farther distance means stronger geometrical attenuation at higher frequencies versus lower frequencies, and thus lower sensitivity to bedload compared to water flow (Gimbert et al., 2014). Also, this station samples a longer river segment because of its farther distance, which could smooth out moving peaks. Moreover, due to the location of the TURF station further to the east, this station can be also influenced by the flood on the Roya river that is located ~ 10 km away from the station. The timing of the main seismic power maximum at the TURF station and the third seismic power maximum of the BELV station are well correlated with the runoff simulations and can be related to the maximum runoff. From maximum 1 to 3, there is a shift from short-lived peaks to a much more spread distribution of power through time. That could be potentially related to different dynamics of the first two maxima (associated with two fast propagating flood waves causing a sudden rise in seismic power) and a progressive increase in the seismic power associated with a progressive increase in the runoff. Finally, the differences between the observed seismic power and the runoff simulations indicate that the simple runoff simulation cannot fully explain the flash-flood dynamics. In future works, seismic observations can provide additional constraints for more accurate rainfall-runoff simulations needed to further investigate the spatio-temporal dynamics of flash floods.

4.2 Earthquake swarm in the Tinée valley

The spatial coincidence between the maximum rainfall of Storm Alex in the Tinée valley and the seismic sequence a few hours later (Figure 1A) raises the question of whether the earthquakes were triggered by the heavy rainfall. Three different hypotheses can be proposed for the triggering of seismicity by meteorological forcing. The first hypothesis is a pore pressure increase at depth caused by fluid migration from the surface through hydraulically connected fractures. In this case, the time lag between rainfall at the surface and earthquakes at depth is dependent on the hydraulic diffusivity along with the fractures (Saar and Manga, 2003; Kraft et al., 2006). The second hypothesis is an elastic stress perturbation in the crust induced by hydrological loadings, such as groundwater level increase after rainfall (Rigo et al., 2008). The third hypothesis is a pore pressure increase in deep fluid-saturated poroelastic rocks in response to overlying hydrological loading (Miller, 2008; D'Agostino et al., 2018).

The time lag between the onset of the rain (October 02, 06:00 UTC) and the onset of the first earthquake swarm (October 4, 00:52 UTC, southern swarm) is $\Delta t = 43$ h. Taking a seismicity depth of $z = 5,000 \text{ m} \pm 2,000 \text{ m}$ below the surface and using a time-distance dependent equation for a propagating pore pressure front, $z = \sqrt{4\pi D \Delta t}$ (Shapiro et al., 1997), we find a hydraulic diffusivity ranging from $D = 4.6$ to $25.2 \text{ m}^2/\text{s}$. This diffusivity range is unrealistically large to indicate earthquakes triggered by fluid migration. Indeed, with such a mechanism, earthquake activity following exceptional rainfall episodes or snowmelt is

characterized by a delay of several days to several months and a lower hydraulic diffusivity ranging from $D=0.01$ to $5.00 \text{ m}^2/\text{s}$ (Kraft et al., 2006; Saar and Manga, 2003; Husen et al., 2007; Montgomery-Brown et al., 2019). Thus, the first hypothesis is unlikely for the first earthquake swarm.

230 The geology of the Tinée valley consists of limestone formations topped by a sandstone layer (Grès d'Annot). These rocks can store large volumes of water, which might support the hypothesis of seismicity triggered by groundwater weight. Rigo et al. (2008) describes earthquake triggering in a karstic (made up of limestone) region at depths smaller than 10 km, 43 h after the onset of heavy rainfall. The authors interpret this earthquake activity as the response of the crust to an elastic stress increase caused by a vertical loading because of the groundwater level rise. On the other hand, Miller (2008) shows that a sharp increase of the hydraulic loading in karst can also produce an instantaneous increase of the pore pressure in the underlying
235 fluid-saturated crust, able to trigger earthquakes.

The resumption of activity of the southern swarm at the same time as the activation of the central swarm (6 days after Storm Alex) and the activation of the northern swarm (22 days after Storm Alex), are more compatible with surface to depth fluid migration. However, as these swarms are at the same depth, this would imply a rather large spatial variation of the hydraulic diffusivity from $D=1.4-7.5 \text{ m}^2/\text{s}$ for the southern and central swarms to $D=0.4-2.0 \text{ m}^2/\text{s}$ for the northern swarm. The
240 successive activation of the three swarms could also suggest an alternative mechanism of triggered seismicity. The northward migration of the seismicity is around 20-30 m/h. This velocity is much greater than 1-10 m/day, usually attributed to fluid diffusion-driven seismicity (e.g., Chen et al., 2012; Ruhl et al., 2016). Yet, this velocity is also lower than velocities reported for aseismic slip-driven seismicity (typically 100-1000 m/h, (e.g., Lohman and McGuire, 2007; Roland and McGuire, 2009; Ruhl et al., 2016; Hatch et al., 2020). However, Chen and Shearer (2011) and Chen et al. (2012) also attribute slow earthquake
245 migration of orders 10-100 m/h to aseismic slip, which are values compatible with velocities we found. Hence the northward migration of the seismicity might highlight the horizontal propagation of an aseismic slip along a fault parallel to the valley. The overlying hydrological loading could trigger this aseismic slip, and its northward propagation could drive the successive rupture of seismic asperities corresponding to the three swarms. The interplay between hydromechanical and aseismic slip processes is increasingly recognized as a driver of earthquake swarms (e.g., de Barros et al., 2020; Hatch et al., 2020). Finally,
250 the seismicity triggered by Storm Alex is collocated with the previous background seismicity, especially at depth (Figure 3). This area of the south-western Alps experiences regular moderate seismic activity. Therefore, the heavy rainfall has likely promoted ruptures on seismogenic structures that could have failed in the longer term. In future studies, measurements of relative seismic velocity changes (" dv/v ", e.g., Brenguier et al. (2008); Illien et al. (2022)) could provide additional insights into the state of the subsurface before, during, and after the storm.

255 5 Conclusions

Our results show that seismometers can constrain interaction between the different Earth's systems, time- and space-dependent processes during the flood, and rainfall-runoff relationship at the catchment scale. That is particularly important in the absence of traditional hydrological measurements, as the study presented here. Observations from permanent seismological stations

in the Maritime Alps provide the timing and velocity propagation of the flood waves. They reveal bedload and turbulence dominated phases of the flood that occurred on the Vésubie River. Our observations also suggest that 114 earthquakes between local magnitude ML 0.5 and 2.5 were triggered by the hydrological loading and/or by the resulting in-situ pore pressure increase in the Tinée valley. Heavy rainfall occurs regularly in autumn in the Mediterranean region, and its intensity is increasing due to climate change (Tramblay and Somot, 2018; Ribes et al., 2019). In the future, installing spatially dense seismic arrays could help further detect and constrain the dynamics of floods and triggered earthquakes (e.g., Meng and Ben-Zion, 2017; Eibl et al., 2020; Chmiel et al., 2021). Finally, the results from this study pave the way to a more detailed analysis of surface and deep Earth processes associated with Storm Alex using the presented unique dataset.

Code and data availability. Obspy Python routines (www.obspy.org) were used to download waveforms and pre-process seismic data. The seismic data is collected under the network code FR (10.15778/RESIF.FR, SPIF, TURF, MVIF stations) and RA (10.15778/RESIF.RA, BELV station) and all seismic data are openly available in the archives of French seismological and geodetic network Résif (<https://seismology.resif.fr/>). The code used for backazimuth analysis can be found in the online supplement of Goodling et al. (2018) paper. Rainfall data (ANTILOPE and COMEPHORE) were provided by Météo-France and are available on request. To gain access please contact Pierre Brigode.

Appendix A: Methods

A1 Seismic power calculation and peak frequency

Stations SPIF, BELV, and TURF are located 1,570, 630, and 5,970 m away from the Vésubie river, respectively. SPIF and TURF are equipped with a 3-component broadband (BB) velocimeter and a 3-component accelerometer, and BELV is only equipped with a 3-component accelerometer. On SPIF and TURF we use the BB recordings for the analysis because of its higher sensitivity than the accelerometer. The sampling frequency for the SPIF and TURF stations is 100 Hz, and the BELV station 125 Hz. Stations BELV and TURF are affected by high-frequency noise that does not allow us to analyse signals higher than 20 Hz. To focus on river-generated seismic signals, we use high-frequency signals (1-50 Hz for SPIF station, and 1-20 Hz for BELV and TURF stations). After the removal of the instrumental response, we first calculate Power Spectral Densities (PSD) splitting the data into 200 s-long time windows with a 50% overlap (in Figures 1D and 2A-C), but no overlap is used in Figures 2E and 2G. The windowing function window is applied to each segment and the PSD is calculated by Welch's average periodogram method (Solomon, 1991a). Then for the SPIF station, we follow previous work on debris flows (Lai et al., 2018) and we investigate signal's peak frequency in individual 200 s time windows between 2-50 Hz. We also analyse seismic power recorded on the SPIF station in two different frequencies bands: 2-10 Hz and 10-45 Hz. For that, we estimate PSD using again Welch's method with time segments of 2 s and no overlap, and then we calculate a median over 30 s time windows.

A2 Azimuth analysis

We perform a frequency-dependent polarization analysis to determine the dominant backazimuth assuming that the seismic signature of the flood is dominated by surface waves on the SPIF station (Goodling et al., 2018). The horizontal azimuth and degree of polarization are determined based on the dominant eigenvector of the spectral covariance matrix of the 3 measured components (N, E and Z), following the approach of Park et al. (2005) and its recent application by Goodling et al. (2018). We determine these variables for 30-minute intervals using 9 subwindows with 50% overlap. The dominant azimuth per frequency (θ) is obtained and given for a range 0-180° as there is a 180° ambiguity in this value.

A3 Rainfall-runoff models

Runoff is firstly estimated using the Soil Conservation Service-Curve Number (SCS-CN) production function method. The SCS-CN function allows to estimate the runoff from a rainfall event depending on the catchment saturation conditions. A simplified unit hydrograph routing function is then used to produce temporal runoff series. This analysis aims at estimating, for each studied catchment, the distances between each Digital Elevation Model (DEM) grid cell and the considered outlet and use the distance to root the runoff at the studied catchment outlets. A distinction is made between the distance travelled on the slopes and the distance travelled in the river (i.e., within the hydrographic network): the flow velocity on the slopes (fixed here at 0.2 m/s) is assumed to be slower than that in the river (fixed here at 5 m/s). These distances are used to calculate, for each grid cell “x” belonging to a studied watershed, the transfer time τ [in (s)] between this grid cell x and the considered outlet:

$$\tau(x) = \frac{L_h(x)}{v_h} + \frac{L_c(x)}{v_c} \quad (\text{A1})$$

where: $L_h(x)$: distance (on the slopes) between the grid cell “x” and the considered catchment outlet (m), v_h : flow velocity on the slopes (m/s), $L_c(x)$: distance (in the river network) between the grid cell “x” and the considered catchment outlet [m], v_c : flow velocity in the river network (m/s).

These transfer times are used to calculate the simulated flow, at time step t, at each studied outlet (denoted Q and expressed in m³/s) by the following expression (no initial base flow is considered in this study):

$$Q(t) = \int_A q(t - \tau(x), x) dx \quad (\text{A2})$$

where: A: catchment area upstream of the grid cell “x” (km²), q: runoff estimated at timestep “t” and at the grid cell “x” (m/s). The runoff is simulated for three locations along the Vésubie river which are the closest to the seismic stations (Figure B3).

A4 Earthquake swarm detection

Previous studies have shown that template matching (e.g., Gibbons and Ringdal, 2006) has a higher detection sensitivity than threshold-based methods such as the STA/LTA used in the Seiscomp3 system. We use template matching to detect low-

magnitude earthquakes that belong to the earthquake swarms. Template matching is performed on the broadband station MVIF (10 km to the south of the swarm). We verified that this station was little affected by the seismic noise generated by the increased river flow during and after the storm. We use the following approach. Data are bandpass filtered in the 5-30 Hz frequency band. We use as templates the 23 earthquakes detected by SeisComp3. The templates are constructed using a 5-s window that includes P and S waves. Next, each template is cross-correlated with daily continuous seismic data. We use only vertical components of the seismograms and we automatically scan the seismic data between September 27 and December 10, 2020. A new earthquake is detected if the cross-correlation coefficient exceeds a threshold of 0.6. This value allows the detection of earthquake waveforms that might slightly differ from the templates (if, for example, the origin location is not the same) while minimizing the number of false detections. Finally, the magnitude of detected earthquakes is estimated from the ratio between its maximum amplitude and the maximum amplitude of the best-correlated template (local magnitude ML). An example of templates and detected events by template matching are presented in Figure B10-B12.

A5 Peak propagation velocity and uncertainty calculation

The peak arrival times are manually picked by taking the beginning of the maximum above fixed seismic power (PSD) thresholds (Figure B4, B9). Also, we verify the time delay between the two PSDs using cross-correlation (Figure B9). We find two maxima of 0.30 and 0.15 at time lag values of 19 and 28 min, respectively. We calculate the peak propagation velocity as a ratio between the distance (d) of the two nearest river coordinates to the SPIF and BELV station (8,012 m) to manually pick the propagation time of the peaks (t). To calculate the distance, we use the nearest river coordinates to the stations, and we integrate the distance following the Vésubie river coordinates (8,012 m). Then, we use error propagation to estimate the uncertainty of the estimated velocity propagation. For that, we use the variance formula assuming that the distance and time measurements are independent:

$$s_v = \sqrt{\left(-\frac{d}{t^2}\right)^2 s_t^2 + \left(\frac{1}{t}\right)^2 s_d^2} \quad (\text{A3})$$

where d is the distance between the two nearest river coordinates to the SPIF and BELV station (8,012 m), t the manually picked propagation time of the peaks (s), s_t the standard deviation of the three propagation times (s): (1) the manually picked propagation time of the peaks, and (2) the two cross-correlation calculated propagation times, s_d the standard deviation of the two distances (m): (1) the distance between the nearest river coordinates to the SPIF and the BELV stations (8,012 m), and (2) the distance of the closest river segment that aligns with the dominant backazimuth calculated at the SPIF station to the closest river coordinates to the BELV station (5,512 m).

Appendix B: Supplemental figures

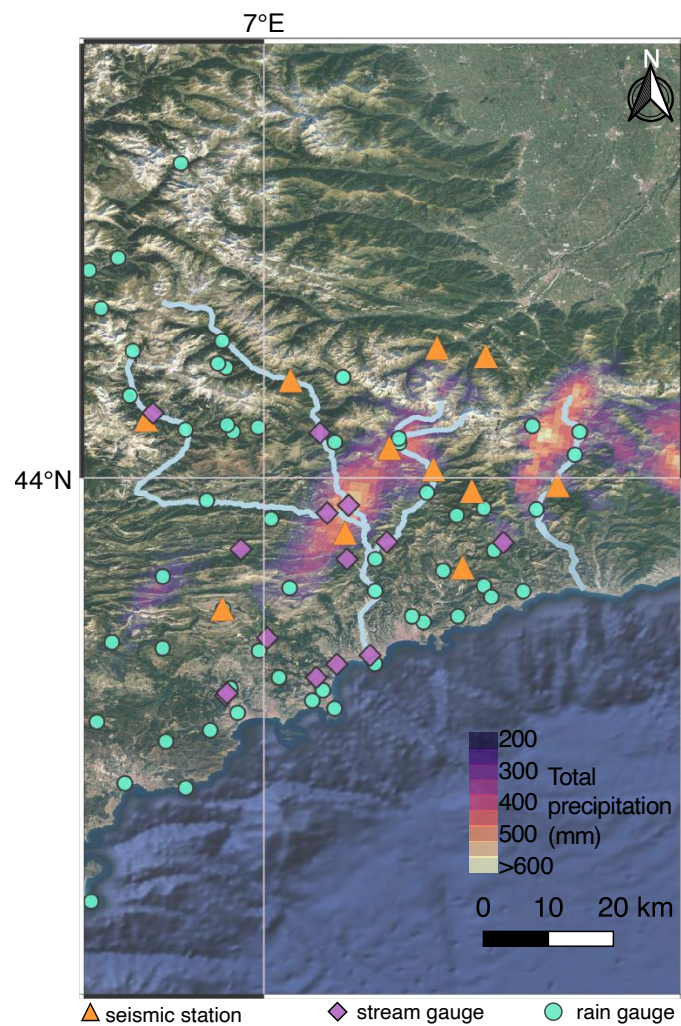


Figure B1. The location of rain and stream gauges and seismic stations in southeastern France.



Figure B2. The consequences of Storm Alex in the Maritime Alps. A. Landslide located upstream from the village of Saint Martin-Vésubie on the right bank of the Boréon river. B. Bank collapse next to the village of Saint Martin-Vésubie. C. Aerial view on the village of Roquebillière Vieux. D. Partial bank collapse and deposited material next to Louvivier village. Photo credits: Florent Adamo/Cerema.

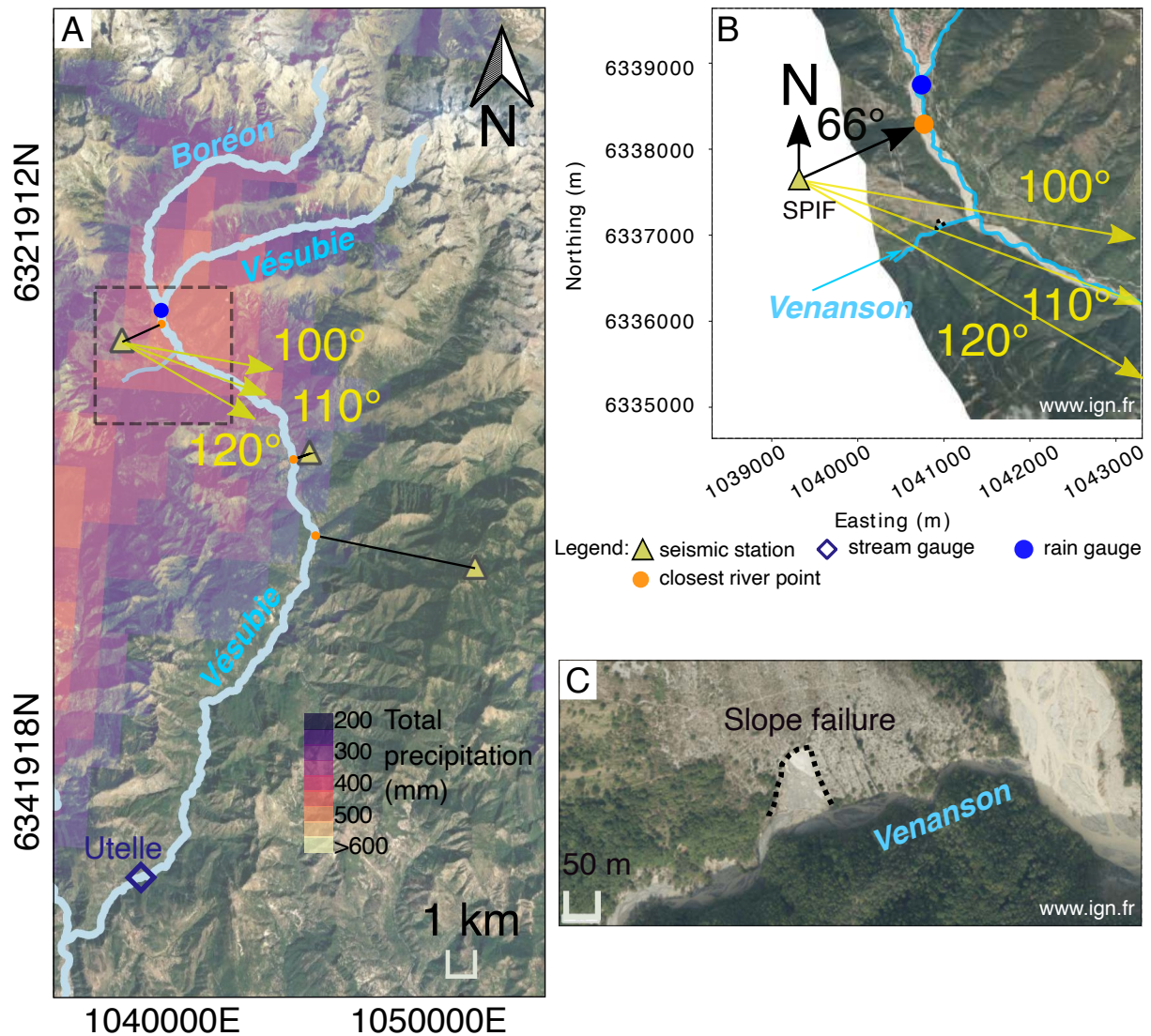


Figure B3. A. Map section showing the Vésubie and the Boréon river. The 25 km² square used for the rainfall calculation in Figure 1B is shown with black dashed lines. Background map source: © Google Maps 2021. B. Zoom on the square marked in panel A. Three dominant azimuth are indicated in yellow arrows showing dominant noise directions of 100°, 110°, and 120° degrees (source: IGN 2020). C. Zoom on the intersection between the Venanson stream and the Vésubie river, with a slope failure indicated that is adjacent to the Venanson stream (source: IGN 2020).

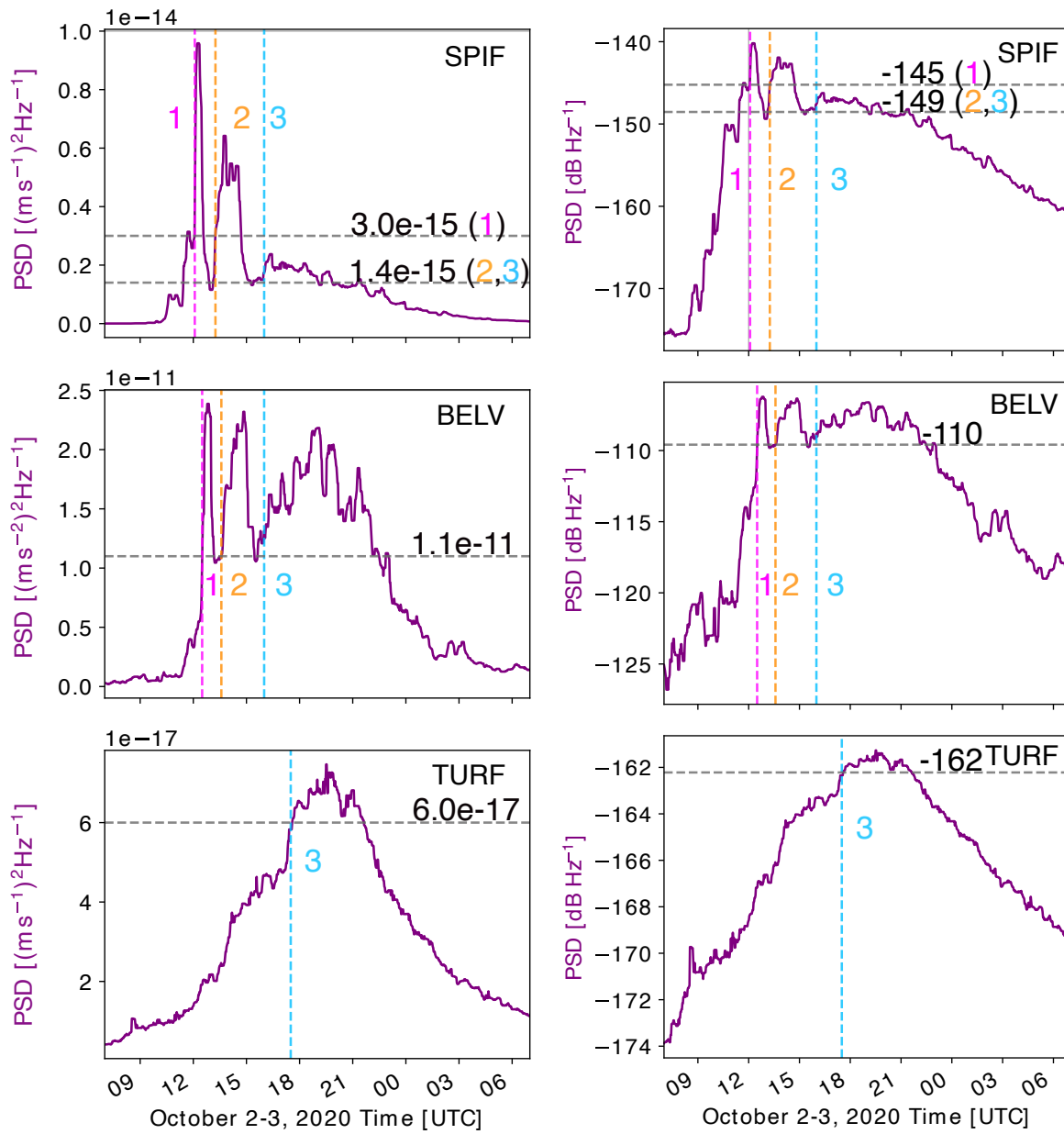


Figure B4. Seismic power (PSD) recorded at SPIF, BELV, and TURF seismic stations in linear scale (left panels) and logarithmic scale (dB, right panels). The seismic power is averaged in 1-20 Hz frequency band, between 07:00 UTC October 2 and 07:00 October 3. Vertical lines show the starting hours of the three peaks, and the horizontal lines show the threshold used to define the peaks.

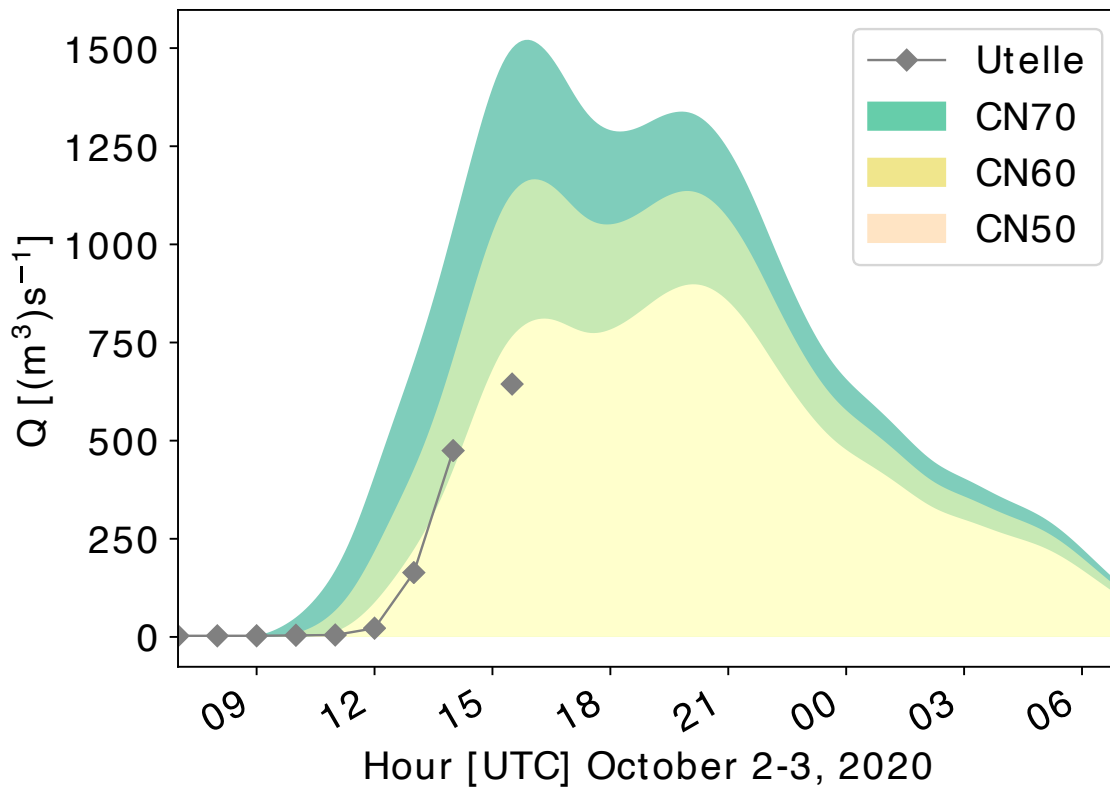


Figure B5. Runoff modeling for three different basin saturation scenarios: CN70 (moderate saturation), CN60, and CN50 (rather dry conditions). Available runoff measurements from the stream gauge at Utelle are presented in gray diamonds. The comparison between the stream gauge measurements and runoff modeling indicates rather dry basin conditions (CN50 scenario). However, there is an uncertainty in the runoff modeling related to the estimated flow velocities on the slope (0.2 m/s) and in the river (5.0 m/s). Moreover, the estimated runoff values are too low comparing to the damage that occurred in the Vésubie catchment.

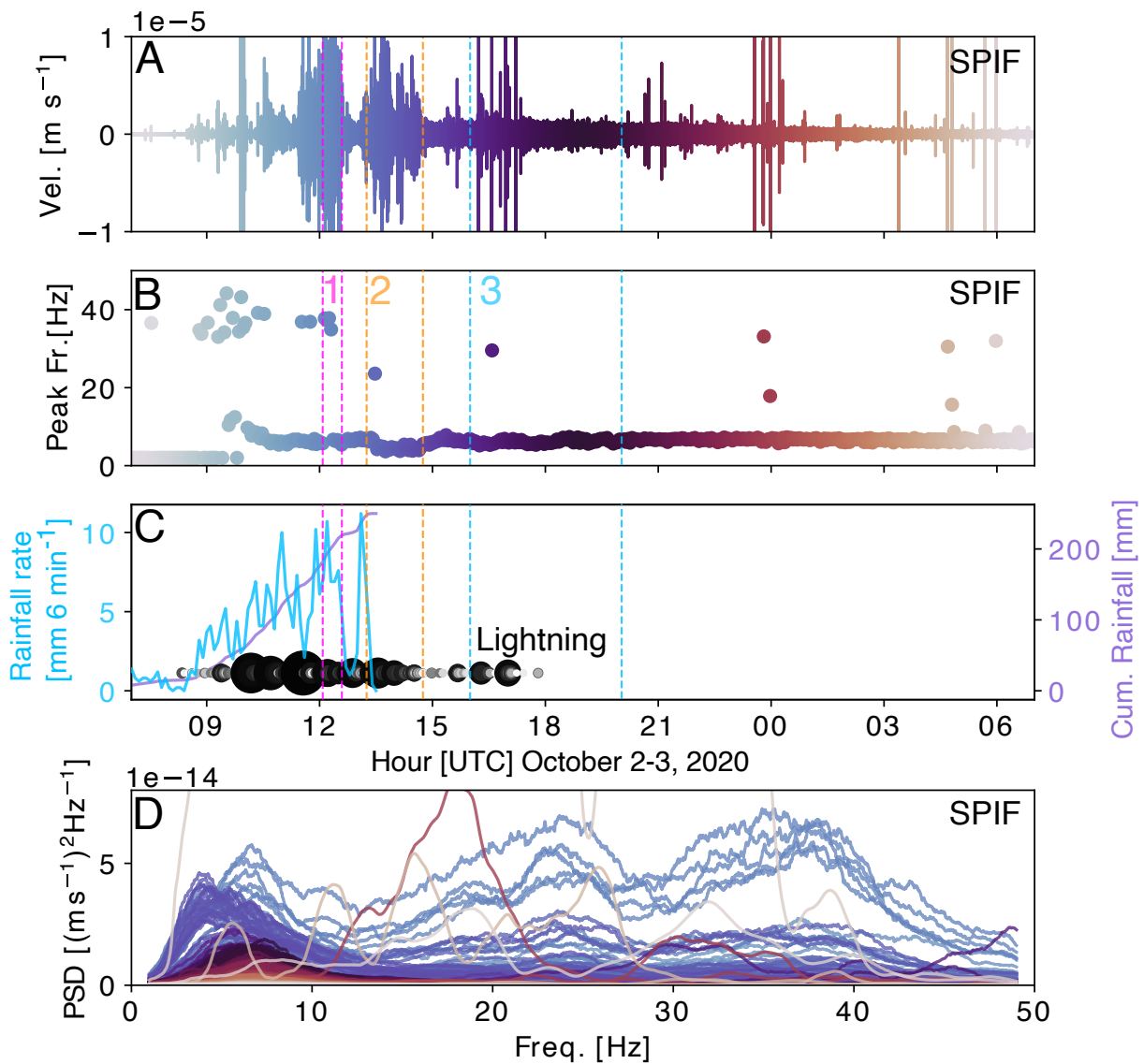


Figure B6. Analysis of seismic data recorded at the SPIF station and meteorological data. A. Vertical ground velocity recorded filtered in 1-50 Hz. B. Peak frequency calculated for each 200 s segment. C. Rainfall measured by the rain gauge at located at Saint-Martin Vésubie. This is the closest rain gauge to the SPIF station located at the distance of 1.9 km. The measurement stopped when the instrument was destroyed. Lightning in the distance <15 km from the SPIF station. Each circle represent a lightening strike, the larger and the darker the circle the closer the lightening. D. Seismic power calculated in windows of 200 s. Peak frequency, corresponding time segment, and seismic power (PSD) are marked in the same color.

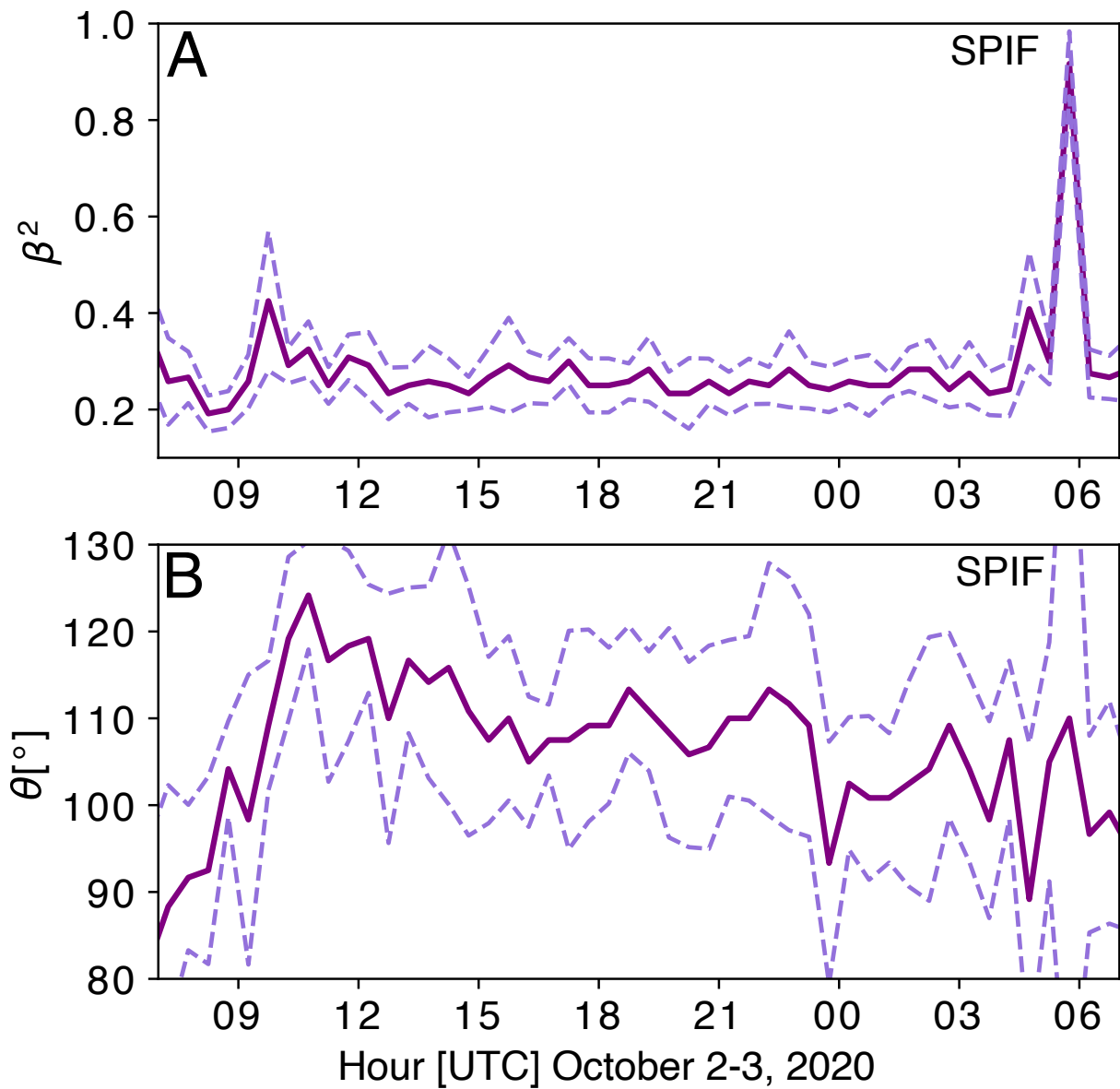


Figure B7. Backazimuth analysis at the SPIF station. A. Non-smoothed polarization degree β^2 . The impulsive high value polarization levels at \sim 06:00 UTC October 3 can be associated with anthropogenic noise sources and there are also visible at different days. B. Non-smoothed backazimuth direction θ , averaged over 3-8 Hz. The mean is shown in continuous line, and the standard deviation in the dashed lines.

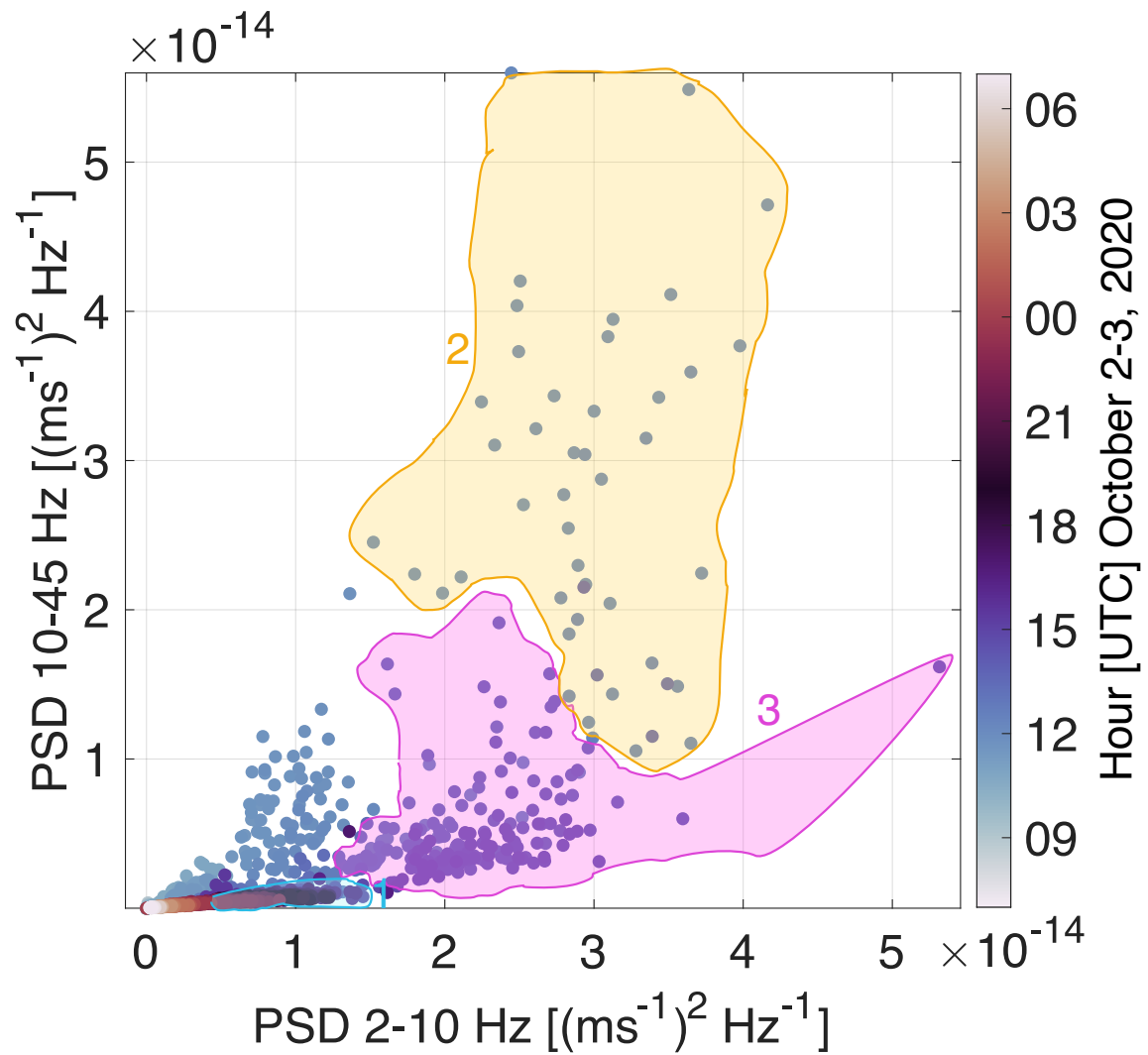


Figure B8. The same plot as Figure 2G, but in the linear scale. Seismic power calculated in 2-10 Hz versus seismic power calculated 10-45 Hz at the SPIF station. The seismic power peaks are marked in different colors.

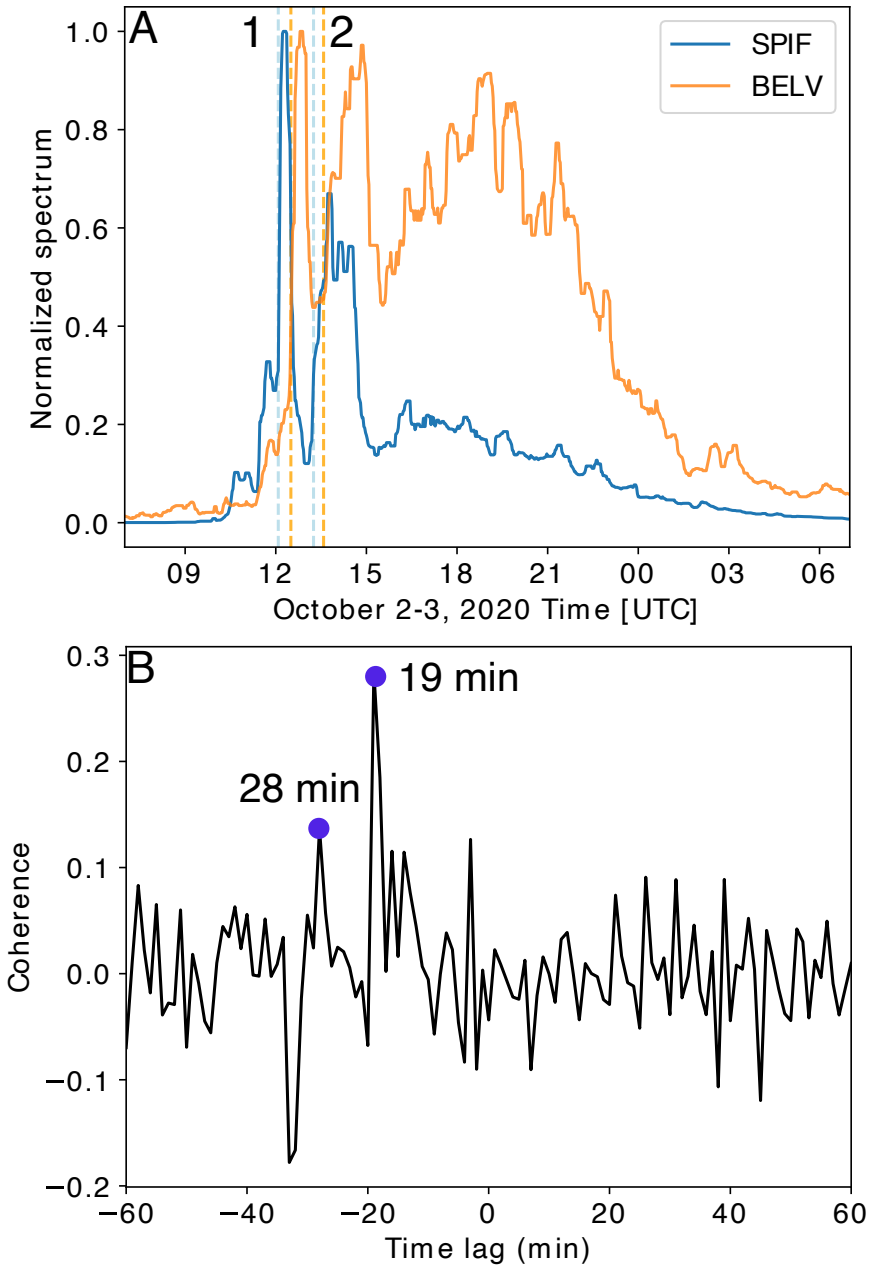


Figure B9. A. Normalized seismic power recorded at the SPIF and the BELV stations smoothed over 30 min moving time average. Arrivals times of peaks 1 and 2 are marked in dashed lines. B. Normalized cross-correlation (coherence) between the normalized seismic power shown in A.

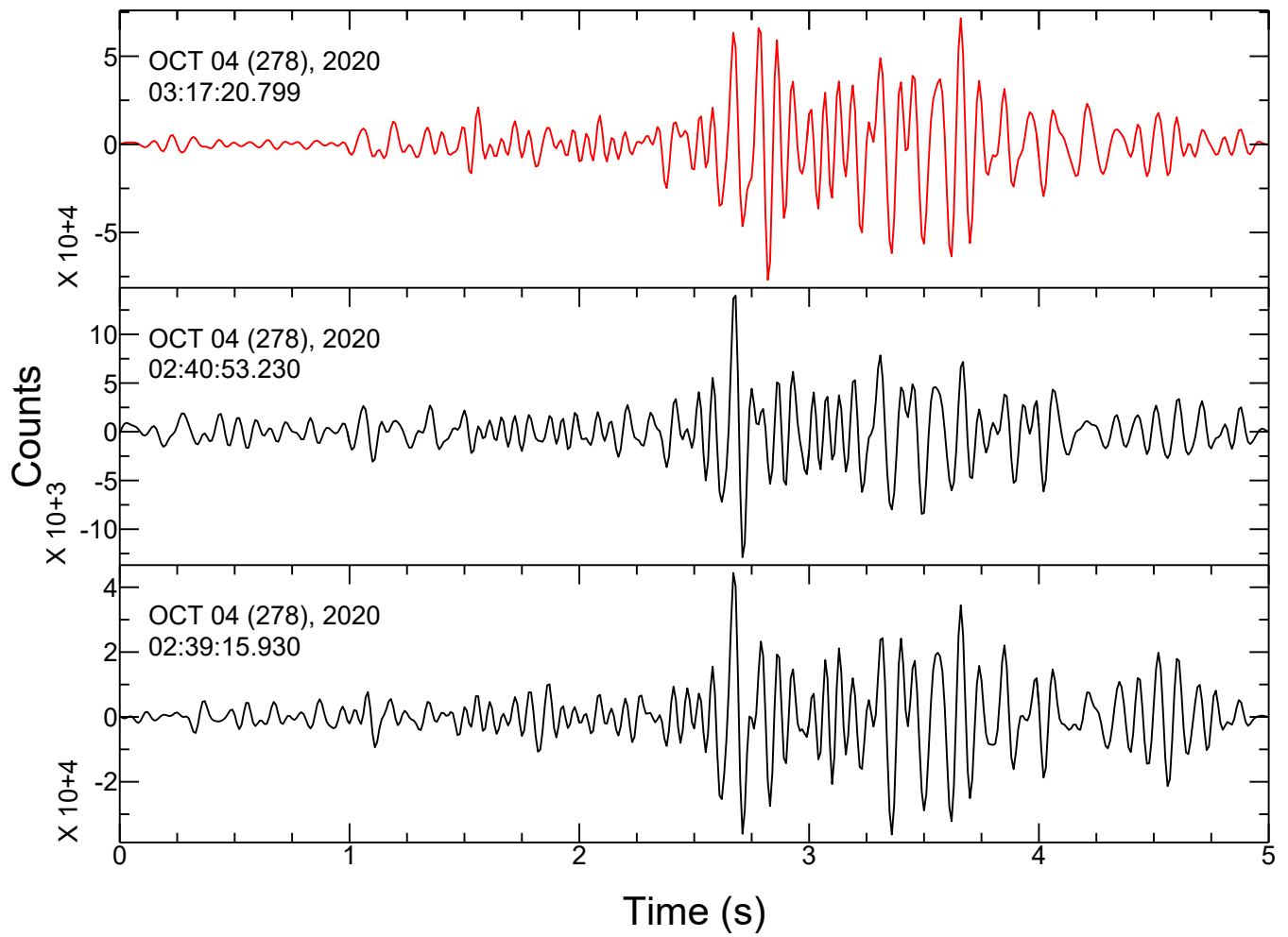


Figure B10. Red: template located in the southern swarm and black: examples of detected events by template matching. Seismograms show vertical ground velocity recorded at the station MVIF and are bandpass-filtered in the range 5-20Hz.

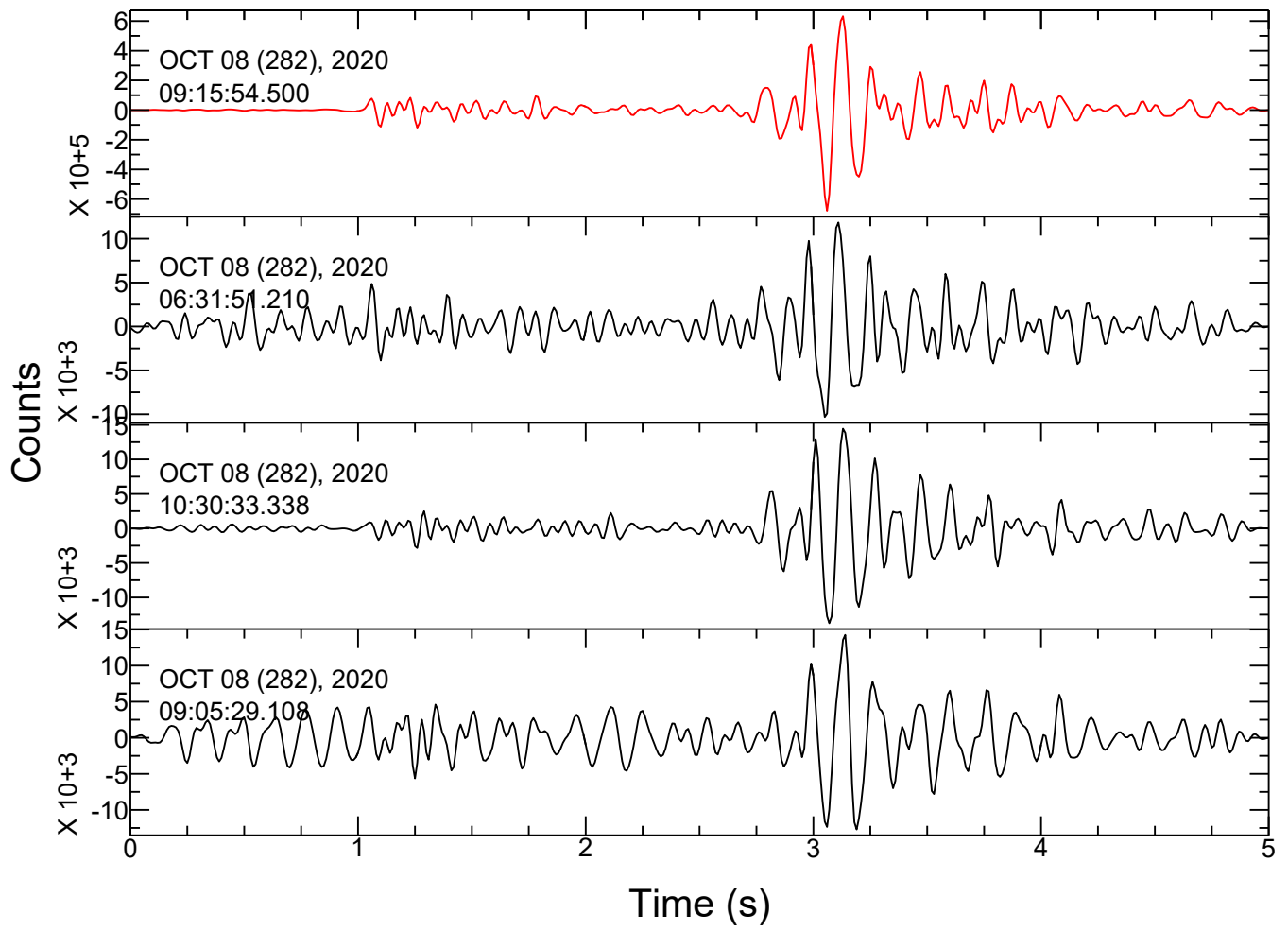


Figure B11. Same as Figure B10, but for a template located in the central swarm.

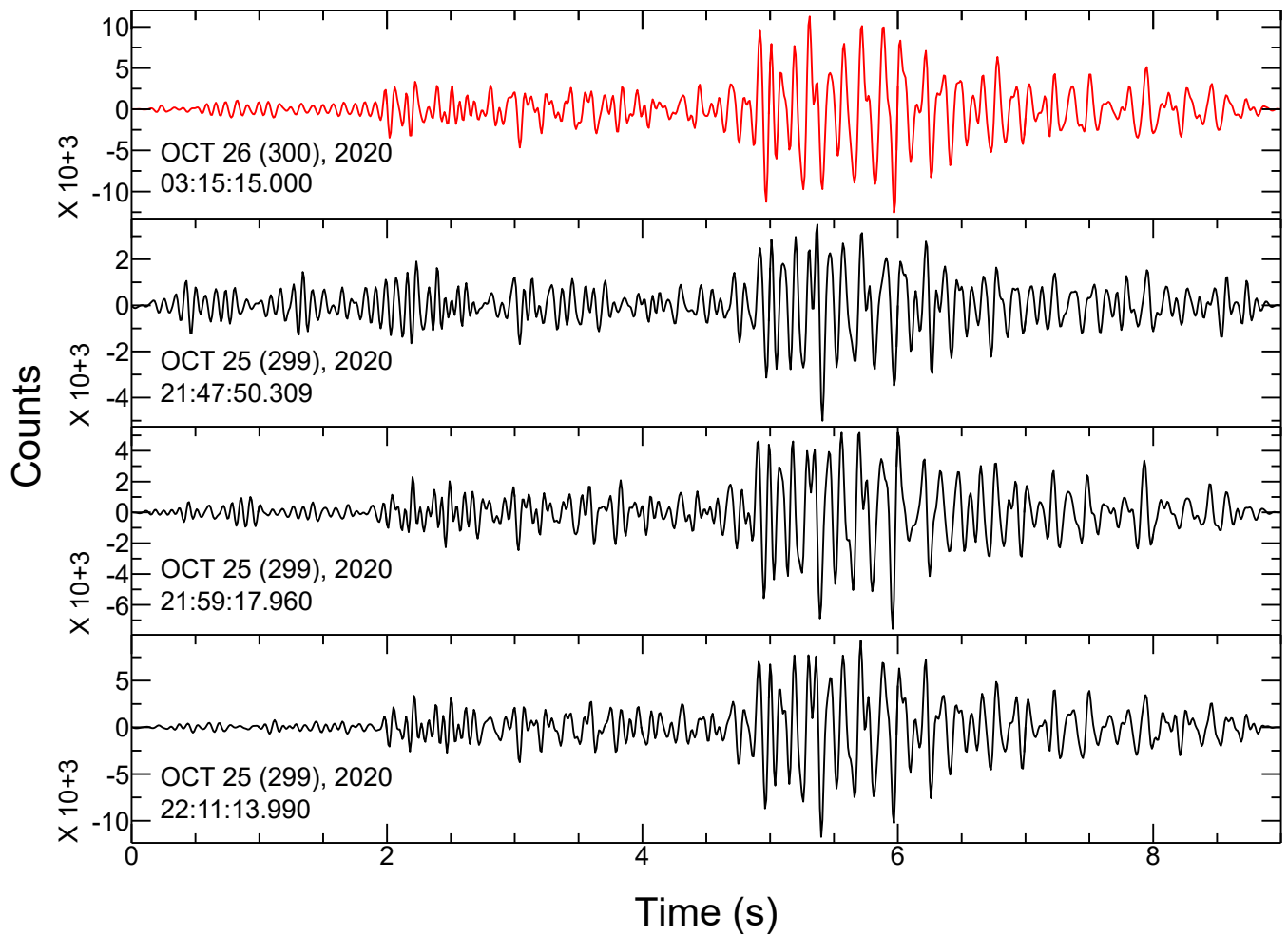


Figure B12. Same as Figure B10, but for a template located in the northern swarm.

Author contributions. MC, MP, MB processed and analyzed the flood seismic data. MG performed the earthquake swarm analysis. PB performed the rainfall-runoff modeling. FG, PB, FC, J-PA, DA, AS, DA, MC helped with the data analysis and interpretation. MC and MG prepared the manuscript with a help of all the co-authors.

Competing interests. The authors declare that they have no conflict of interest.

Acknowledgements. We thank Observatoire de la Côte d'Azur that partially founded this work. We also thank the ANR project ANR SEIS-MORIV ANR-17-CE01-0008 granted to FG. We thank Didier Brunel, Christophe Maron, Jerome Cheze and all the persons in charge of

350 the permanent seismic network and data. We thank Florent Adamo and Cerema for kindly allowing us to use their photos. We thank two anonymous Reviewers for their helpful review and valuable comments.

References

- Aki, K. and Richards, P. G.: Quantitative Seismology, University Science Books, 2 edn., <http://www.worldcat.org/isbn/0935702962>, 2002.
- Bakker, M., Gimbert, F., Geay, T., Misset, C., Zanker, S., and Recking, A.: Field Application and Validation of a Seismic Bedload Transport Model, *Journal of Geophysical Research: Earth Surface*, 125, e2019JF005416, <https://doi.org/https://doi.org/10.1029/2019JF005416>,
355 _eprint: <https://agupubs.onlinelibrary.wiley.com/doi/pdf/10.1029/2019JF005416>, 2020.
- Borga, M., Boscolo, P., Zanon, F., and Sangati, M.: Hydrometeorological Analysis of the 29 August 2003 Flash Flood in the Eastern Italian Alps, *Journal of Hydrometeorology*, 8, 1049 – 1067, <https://doi.org/10.1175/JHM593.1>, 2007.
- Borga, M., Comiti, F., Ruin, I., and Marra, F.: Forensic analysis of flash flood response, *WIREs Water*, 6, e1338,
360 <https://doi.org/10.1002/wat2.1338>, _eprint: <https://wires.onlinelibrary.wiley.com/doi/pdf/10.1002/wat2.1338>, 2019.
- Brenguier, F., Campillo, M., Hadziioannou, C., Shapiro, N. M., Nadeau, R. M., and Larose, É.: Postseismic Relaxation Along the San Andreas Fault at Parkfield from Continuous Seismological Observations, *Science*, 321, 1478 – 1481, 2008.
- Brigode, P., Vigoureux, S., Delestre, O., Nicolle, P., Payrastre, O., Dreyfus, R., Nomis, S., and Salvan, L.: Inondations sur la Côte d'Azur : bilan hydro-météorologique des épisodes de 2015 et 2019, *La Houille Blanche*, in submission., –, <https://doi.org/>, 2021a.
- 365 Brigode, P., Vigoureux, S., Delestre, O., Nicolle, P., Payrastre, O., Dreyfus, R., Nomis, S., and Salvan, L.: Inondations sur la Côte d'Azur : bilan hydro-météorologique des épisodes de 2015 et 2019, <https://doi.org/10.1080/27678490.2021.1976600>, 2021b.
- Burtin, A., Cattin, R., Bollinger, L., Vergne, J., Steer, P., Robert, A., Findling, N., and Tiberi, C.: Towards the hydrologic and bed load monitoring from high-frequency seismic noise in a braided river: The “torrent de St Pierre”, French Alps, *Journal of Hydrology*, 408, 43–53, <https://doi.org/10.1016/j.jhydrol.2011.07.014>, 2011.
- 370 Burtin, A., Hovius, N., and Turowski, J. M.: Seismic monitoring of torrential and fluvial processes, *Earth Surface Dynamics*, 4, 285–307, <https://doi.org/10.5194/esurf-4-285-2016>, 2016.
- Carrega, P. and Michelot, N.: Une catastrophe hors norme d'origine météorologique le 2 octobre 2020 dans les montagnes des Alpes-Maritimes, *Physio-Géo*, 16, 1–70, <https://doi.org/10.4000/physio-geo.12370>, 2021.
- Chen, X. and Shearer, P. M.: Comprehensive analysis of earthquake source spectra and swarms in the Salton Trough, California, *Journal of Geophysical Research*, 116, 2011.
- 375 Chen, X., Shearer, P. M., and Abercrombie, R. E.: Spatial migration of earthquakes within seismic clusters in Southern California: Evidence for fluid diffusion, *Journal of Geophysical Research: Solid Earth*, 117, <https://doi.org/https://doi.org/10.1029/2011JB008973>, 2012.
- Chmiel, M., Walter, F., Wenner, M., Zhang, Z., McArdell, B. W., and Hibert, C.: Machine Learning Improves Debris Flow Warning, *Geophysical Research Letters*, 48, e2020GL090874, <https://doi.org/10.1029/2020GL090874>, _eprint:
380 <https://agupubs.onlinelibrary.wiley.com/doi/pdf/10.1029/2020GL090874>, 2021.
- Cook, K. L., Andermann, C., Gimbert, F., Adhikari, B. R., and Hovius, N.: Glacial lake outburst floods as drivers of fluvial erosion in the Himalaya, *Science*, 362, 53–57, <https://doi.org/10.1126/science.aat4981>, publisher: American Association for the Advancement of Science Section: Report, 2018.
- Cook, K. L., Rekapalli, R., Dietze, M., Pilz, M., Cesca, S., Rao, N. P., Srinagesh, D., Paul, H., Metz, M., Mandal, P., Suresh, G., Cotton, F.,
385 Tiwari, V. M., and Hovius, N.: Detection and potential early warning of catastrophic flow events with regional seismic networks, *Science*, 374, 87–92, <https://doi.org/10.1126/science.abj1227>, 2021.
- Costain, J. K. and Bollinger, G. A.: Review: Research results in hydroseismicity from 1987 to 2009, *Bulletin of the Seismological Society of America*, 100, 1841–1858, <https://doi.org/https://doi.org/10.1785/0120090288>, 2010.

- 390 D'Agostino, N., Silverii, F., Amoroso, O., Convertito, V., Fiorillo, F., Ventafridda, G., and Zollo, A.: Crustal Deformation and Seismicity Modulated by Groundwater Recharge of Karst Aquifers, *Geophysical Research Letters*, 45, 12,253–12,262, <https://doi.org/https://doi.org/10.1029/2018GL079794>, 2018.
- de Barros, L., Cappa, F., Deschamps, A., and Dublanchet, P.: Imbricated Aseismic Slip and Fluid Diffusion Drive a Seismic Swarm in the Corinth Gulf, Greece, *Geophysical Research Letters*, 47, 2020.
- 395 Eibl, E. P. S., Bean, C. J., Einarsson, B., Pålsson, F., and Vogfjörð, K. S.: Seismic ground vibrations give advanced early-warning of subglacial floods, *Nature Communications*, 11, 2504, <https://doi.org/10.1038/s41467-020-15744-5>, 2020.
- Gibbons, S. J. and Ringdal, F.: The detection of low magnitude seismic events using array-based waveform correlation, *Geophysical Journal International*, 165, 149–166, <https://doi.org/10.1111/j.1365-246X.2006.02865.x>, 2006.
- Gimbert, F., Tsai, V., and Lamb, M.: A physical model for seismic noise generation by turbulent flow in rivers, *J. Geophys. Res. Earth Surf.*, 119, 2209–2238, <https://doi.org/https://doi.org/10.1002/2014JF003201>, 2014.
- 400 Gimbert, F., Fuller, B. M., Lamb, M. P., Tsai, V. C., and Johnson, J. P. L.: Particle transport mechanics and induced seismic noise in steep flume experiments with accelerometer-embedded tracers, *Earth Surf. Process. Landforms*, 44, 219–241, <https://doi.org/https://doi.org/10.1002/esp.4495>, 2019.
- Goodling, P. J., Lekic, V., and Prestegard, K.: Seismic signature of turbulence during the 2017 Oroville Dam spillway erosion crisis, *Earth Surface Dynamics*, 6, 351–367, <https://doi.org/10.5194/esurf-6-351-2018>, publisher: Copernicus GmbH, 2018.
- 405 Hainzl, S., Kraft, T., Wassermann, J., Igel, H., and Schmedes, E.: Evidence for rainfall-triggered earthquake activity, *Geophysical Research Letters*, 33, <https://doi.org/https://doi.org/10.1029/2006GL027642>, 2006.
- Hanka, W., Saul, J., Weber, B., Becker, J., Harjadi, P., Fauzi, and Group, G. S.: Real-time earthquake monitoring for tsunami warning in the Indian Ocean and beyond, *Natural Hazards and Earth System Sciences*, 10, 2611–2622, <https://doi.org/10.5194/nhess-10-2611-2010>, 2010.
- 410 Hatch, R. L., Abercrombie, R. E., Ruhl, C. J., and Smith, K. D.: Evidence of Aseismic and Fluid-Driven Processes in a Small Complex Seismic Swarm Near Virginia City, Nevada, *Geophysical Research Letters*, 47, 2020.
- Hsu, Y.-J., Kao, H., Bürgmann, R., Lee, Y.-T., Huang, H.-H., Hsu, Y.-F., Wu, Y.-M., and Zhuang, J.: Synchronized and asynchronous modulation of seismicity by hydrological loading: A case study in Taiwan, *Science Advances*, 7, eabf7282, <https://doi.org/10.1126/sciadv.abf7282>, 2021.
- 415 Husen, S., Bachmann, C., and Giardini, D.: Locally triggered seismicity in the central Swiss Alps following the large rainfall event of August 2005, *Geophysical Journal International*, 171, 1126–1134, <https://doi.org/10.1111/j.1365-246X.2007.03561.x>, 2007.
- Illien, L., Sens-Schönfelder, C., Andermann, C., Marc, O., Cook, K. L., Adhikari, L. B., and Hovius, N.: Seismic velocity recovery in the subsurface: transient damage and groundwater drainage following the 2015 Gorkha earthquake, Nepal, *Journal of Geophysical Research: Solid Earth*, 2022.
- 420 IPCC: Summary for Policymakers, Cambridge University Press, Cambridge, United Kingdom and New York, NY, USA, https://www.ipcc.ch/report/ar6/wg1/downloads/report/IPCC_AR6_WGI_SPM_final.pdf, In Press.
- Johnson, C. W., Fu, Y., and BÄErgmann, R.: Seasonal water storage, stress modulation, and California seismicity, *Science*, 356, 1161–1164, <https://doi.org/10.1126/science.aak9547>, 2017.
- 425 Khajehei, S., Ahmadalipour, A., Shao, W., and Moradkhani, H.: A Place-based Assessment of Flash Flood Hazard and Vulnerability in the Contiguous United States, *Scientific Reports*, 10, 448, <https://doi.org/10.1038/s41598-019-57349-z>, bandiera_abtest: a Cc_license_type:

- cc_by Cg_type: Nature Research Journals Number: 1 Primary_atype: Research Publisher: Nature Publishing Group Subject_term: Hydrology;Natural hazards Subject_term_id: hydrology;natural-hazards, 2020.
- Koper, K. D. and Hawley, V. L.: Frequency dependent polarization analysis of ambient seismic noise recorded at a broadband seismometer in the central United States, *Earthquake Science*, 23, 439–447, <https://doi.org/10.1007/s11589-010-0743-5>, 2010.
- 430 Kraft, T., Wassermann, J., Schmedes, E., and Igel, H.: Meteorological triggering of earthquake swarms at Mt. Hochstaufen, SE-Germany, *Tectonophysics*, 424, 245–258, <https://doi.org/https://doi.org/10.1016/j.tecto.2006.03.044>, dynamics of Seismicity Patterns and Earthquake Triggering, 2006.
- Kundu, B., Vissa, N. K., Panda, D., Jha, B., Asaithambi, R., Tyagi, B., and Mukherjee, S.: Influence of a meteorological cycle in mid-crustal seismicity of the Nepal Himalaya, *Journal of Asian Earth Sciences*, 146, 317–325, <https://doi.org/https://doi.org/10.1016/j.jseaes.2017.06.003>, 2017.
- 435 Lagarde, S., Dietze, M., Gimbert, F., Laronne, J. B., Turowski, J. M., and Halfi, E.: Grain-Size Distribution and Propagation Effects on Seismic Signals Generated by Bedload Transport, *Water Resources Research*, 57, e2020WR028700, <https://doi.org/https://doi.org/10.1029/2020WR028700>, e2020WR028700 2020WR028700, 2021.
- Lai, V. H., Tsai, V. C., Lamb, M. P., Ulizio, T. P., and Beer, A. R.: The Seismic Signature of Debris Flows: Flow Mechanics and Early
440 Warning at Montecito, California, *Geophysical Research Letters*, 45, 5528–5535, <https://doi.org/10.1029/2018GL077683>, 2018.
- Laurantin, O.: ANTILOPE: Hourly rainfall analysis merging radar and rain gauge data. *Proceedings of the International Symposium on Weather Radar and Hydrology*, pp. 2–8, 2008.
- Lohman, R. B. and McGuire, J. J.: Earthquake swarms driven by aseismic creep in the Salton Trough, California, *Journal of Geophysical Research*, 112, 2007.
- 445 Maurer, J. M., Schaefer, J. M., Russell, J. B., Rupper, S., Wangdi, N., Putnam, A. E., and Young, N.: Seismic observations, numerical modeling, and geomorphic analysis of a glacier lake outburst flood in the Himalayas, *Science Advances*, 6, eaba3645, <https://doi.org/10.1126/sciadv.aba3645>, 2020.
- Meng, H. and Ben-Zion, Y.: Detection of small earthquakes with dense array data: example from the San Jacinto fault zone, southern California, *Geophysical Journal International*, 212, <https://doi.org/10.1093/gji/ggx404>, 2017.
- 450 Miller, S. A.: Note on rain-triggered earthquakes and their dependence on karst geology, *Geophysical Journal International*, 173, 334–338, <https://doi.org/10.1111/j.1365-246X.2008.03735.x>, 2008.
- Montgomery-Brown, E. K., Shelly, D. R., and Hsieh, P. A.: Snowmelt-Triggered Earthquake Swarms at the Margin of Long Valley Caldera, California, *Geophysical Research Letters*, 46, 3698–3705, <https://doi.org/https://doi.org/10.1029/2019GL082254>, 2019.
- Park, C. B., Miller, R. D., and Xia, J.: Imaging dispersion curves of surface waves on multi-channel record, pp. 1377–1380,
455 <https://doi.org/10.1190/1.1820161>, 2005.
- Piantini, M., Gimbert, F., Bellot, H., and Recking, A.: Triggering and propagation of exogenous sediment pulses in mountain channels: insights from flume experiments with seismic monitoring, *Earth Surface Dynamics*, 9, 1423–1439, <https://doi.org/10.5194/esurf-9-1423-2021>, 2021.
- Raynaud, D., Thielen, J., Salamon, P., Burek, P., Anquetin, S., and Alfieri, L.: A dynamic runoff co-efficient to improve flash flood
460 early warning in Europe: evaluation on the 2013 central European floods in Germany, *Meteorological Applications*, 22, 410–418, <https://doi.org/10.1002/met.1469>, _eprint: <https://rmets.onlinelibrary.wiley.com/doi/pdf/10.1002/met.1469>, 2015.
- Ribes, A., Thao, S., Vautard, R., Dubuisson, B., Somot, S., Colin, J., Planton, S., and Soubeyroux, J.-M.: Observed increase in extreme daily rainfall in the French Mediterranean, *Climate Dynamics*, 52, 1095–1114, <https://doi.org/10.1007/s00382-018-4179-2>, 2019.

- Rigo, A., Béthoux, N., Masson, F., and Ritz, J.-F.: Seismicity rate and wave-velocity variations as consequences of rainfall: The case of the catastrophic storm of September 2002 in the Nîmes Fault region (Gard, France), *Geophys. J. Int.*, 173, 473–482, <https://doi.org/10.1111/j.1365-246X.2008.03718.x>, 2008.
- Roland, E. and McGuire, J. J.: Earthquake swarms on transform faults, *Geophysical Journal International*, 178, 1677–1690, 2009.
- Roth, D. L., Brodsky, E. E., Finnegan, N. J., Rickenmann, D., Turowski, J. M., and Badoux, A.: Bed load sediment transport inferred from seismic signals near a river, *Journal of Geophysical Research: Earth Surface*, 121, 725–747, <https://doi.org/10.1002/2015JF003782>,
_eprint: <https://agupubs.onlinelibrary.wiley.com/doi/pdf/10.1002/2015JF003782>, 2016.
- Roth, D. L., Finnegan, N. J., Brodsky, E. E., Rickenmann, D., Turowski, J. M., Badoux, A., and Gimbert, F.: Bed load transport and boundary roughness changes as competing causes of hysteresis in the relationship between river discharge and seismic amplitude recorded near a steep mountain stream, *Journal of Geophysical Research: Earth Surface*, 122, 1182–1200, <https://doi.org/https://doi.org/10.1002/2016JF004062>, 2017.
- Roth, P., Pavoni, N., and Deichmann, N.: Seismotectonics of the eastern Swiss Alps and evidence for precipitation-induced variations of seismic activity, *Tectonophysics*, 207, 183–197, [https://doi.org/https://doi.org/10.1016/0040-1951\(92\)90477-N](https://doi.org/https://doi.org/10.1016/0040-1951(92)90477-N), the European Geotraverse, Part 8, 1992.
- Ruhl, C. J., Abercrombie, R. E., Smith, K. D., and Zaliapin, I.: Complex Spatiotemporal Evolution of the 2008 Mw 4.9 Mogul Earthquake Swarm (Reno, Nevada): Interplay of Fluid and Faulting, *Journal of Geophysical Research*, 121, 8196–8216, 2016.
- Saar, M. O. and Manga, M.: Seismicity induced by seasonal groundwater recharge at Mt. Hood, Oregon, *Earth and Planetary Science Letters*, 214, 605–618, [https://doi.org/https://doi.org/10.1016/S0012-821X\(03\)00418-7](https://doi.org/https://doi.org/10.1016/S0012-821X(03)00418-7), 2003.
- Schmandt, B., Aster, R. C., Scherler, D., Tsai, V. C., and Karlstrom, K.: Multiple fluvial processes detected by riverside seismic and infrasound monitoring of a controlled flood in the Grand Canyon, *Geophysical Research Letters*, 40, 4858–4863, <https://doi.org/10.1002/grl.50953>,
_eprint: <https://agupubs.onlinelibrary.wiley.com/doi/pdf/10.1002/grl.50953>, 2013.
- Schmandt, B., Gaeuman, D., Stewart, R., Hansen, S., Tsai, V., and Smith, J.: Seismic array constraints on reach-scale bedload transport, *Geology*, 45, 299–302, <https://doi.org/10.1130/G38639.1>, 2017.
- Shapiro, S. A., Huenges, E., and Borm, G.: Estimating the crust permeability from fluid-injection-induced seismic emission at the KTB site, *Geophysical Journal International*, 131, F15–F18, <https://doi.org/10.1111/j.1365-246X.1997.tb01215.x>, 1997.
- Solomon, J.: PSD computations using Welch’s method. [Power Spectral Density (PSD)], Tech. Rep. SAND-91-1533, Sandia National Labs., Albuquerque, NM (United States), <https://doi.org/10.2172/5688766>, 1991a.
- Solomon, Jr, O. M.: PSD computations using Welch’s method. [Power Spectral Density (PSD)], <https://doi.org/10.2172/5688766>, 1991b.
- Stoffel, M. and Huggel, C.: Effects of climate change on mass movements in mountain environments, *Progress in Physical Geography: Earth and Environment*, 36, 421–439, <https://doi.org/10.1177/0309133312441010>, 2012.
- Tabary, P., Dupuy, P., L’HEenaff, G., Gueguen, C., Moulin, L., Laurantin, O., Merlier, C., and J.-M., S.: A 10-year (1997–2006) reanalysis of Quantitative Precipitation Estimation over France: methodology and first results, vol. 1, pp. 255–260, International Association of Hydrological Sciences, Wallingford, United Kingdom, 2012.
- Tramblay, Y. and Somot, S.: Future evolution of extreme precipitation in the Mediterranean, *Climatic Change*, 151, 289–302, <https://doi.org/10.1007/s10584-018-2300-5>, 2018.
- Tsai, V. C., Minchew, B., Lamb, M. P., and Ampuero, J.-P.: A physical model for seismic noise generation from sediment transport in rivers, *Geophysical Research Letters*, 39, <https://doi.org/https://doi.org/10.1029/2011GL050255>,
_eprint: <https://agupubs.onlinelibrary.wiley.com/doi/pdf/10.1029/2011GL050255>, 2012.

Ueda, T. and Kato, A.: Seasonal Variations in Crustal Seismicity in San-in District, Southwest Japan, *Geophysical Research Letters*, 46, 3172–3179, <https://doi.org/https://doi.org/10.1029/2018GL081789>, 2019.

505 Zhang, Z., Walter, F., McArdell, B. W., Wenner, M., Chmiel, M., de Haas, T., and He, S.: Insights From the Particle Impact Model Into the High-Frequency Seismic Signature of Debris Flows, *Geophysical Research Letters*, 48, e2020GL088994, <https://doi.org/https://doi.org/10.1029/2020GL088994>, e2020GL088994 2020GL088994, 2021.